ANALYSIS OF DEFECT STRUCTURES IN HIGH PURITY COPPER SINGLE CRYSTALS USING X-RAY TOPOGRAPHIC TECHNIQUES

by

Gregory P. Hamill

In Partial Fulfillment of the Requirements for the Degree of Doctor of Philosophy

California Institute of Technology
Pasadena, California

1978

(submitted September 12, 1977)

To my wife, Nancy, and

in memory of my parents

ACKNOWLEDGEMENTS

The author wishes to thank Dr. Thad Vreeland, Jr. for his support, guidance, and assistance throughout the research program. Dr. David S. Wood often enlightened the author with solutions to questions or problems. Conversations with and feedback from Drs. Tom Hughes, and Silvanus S. Lau are greatly appreciated. Work completed by previous doctoral students and other researchers in Keck Laboratories, notably Drs. K. M. Jassby, D. B. Pope, L. Tu, and A. P. L. Turner, provided excellent background upon which the present research is based.

The Central Machine Shop and the Glass Blowing Shop of California Institute of Technology gave consistantly good service and assistance in designing. Robert H. Seltzer, of the Jet Propulsion Laboratory, image processed the distorted negatives of the topographs.

Acknowledgement must be given to the United States government for several National Defense and Education Act scholarships and for Department of the Army research grants. The tuition scholarships provided by California Institute of Technology not only supported the author financially but also supplied experience in education and research.

Recognition is well deserved for the hard work undertaken by Alvin Illig in all parts of the research.

The author must also thank his wife for surviving.

ABSTRACT

Copper single crystals were grown in a modified Czochralski system. The "grown-in" dislocations and those introduced through selective scratching of the polished (111) surfaces were observed using Berg-Barrett X-ray topography and Borrmann transmission topographic methods.

Several aspects of the dislocation images may be understood on the basis of pure dynamical or kinematical theories of X-ray diffraction. Some observations, however, support the theory that both dynamical and kinematic effects must be considered to properly describe the experimental results.

Stereo depth measurements of the dislocation images were taken under four sets of X-ray geometries. The minimum range of depths observed, approximately 1.0 to 2.0 μm from the surface, was obtained for both methods of Berg-Barrett stereo topography. The Borrmann transmission topographs provided an image depth range of approximately 3.0 μm from the exit surface to 270 μm from the exit surface. This latter value is equivalent to the crystal thickness, to the accuracy of the present data. Comparison of reflection (Berg-Barrett) and transmission (Borrmann) topographs of the same crystal showed that no image of an individual dislocation on one topograph had a corresponding image on the second topograph.

An attempt to mark the surface of the crystal by vapor

depositing gold dot "absorbers" on the surface was not completely satisfactory due to a shadowing effect in Berg-Barrett topography. The apparent epitaxial growth of the gold dots on the (111) copper surface and the corresponding strain field in the crystal around the dots provided a reference surface for transmission topography, although the true surface was marked only in the asymmetric stereo topographs.

Computer simulation using finite element analysis is proposed to solve the problems of X-ray image formation.

TABLE OF CONTENTS

LIST OF TABLES

LIST OF FIGURES

I. INTRODUCTION

Direct observations of the three dimensional geometry of dislocations using non-destructive procedures is critical in the study of microscopic stress-strain properties of a material. Information on dislocation motions in response to applied stress and the methods of observation of the defects in this laboratory is fairly extensive (A.P.L. Turner, T. Vreeland, Jr., D.B. Pope, 1968; D.B. Pope, T. Vreeland, Jr., 1969; K.M. Jassby, T. Vreeland, Jr., 1970, 1973; L.K. Tu, T. Vreeland, Jr., 1974; T. Vreeland, Jr., 1976). To extend the research to dislocation velocities nearer the velocity of sound in the crystal required advances in three directions. First, a short stress pulse was essential to reduce the total dislocation motion so that the individual dislocation can still be distinguished from other dislocations. Second, crystals with very low initial dislocation density were required to aid in the observation of specific dislocations. Third, improved X-ray topographic methods for observing the three dimensional orientation of dislocations in crystals had to be developed. This paper details research on the last two proposed directions.

The Czochralski technique of crystal growth has been shown to be a better method than the Bridgeman technique for growth of copper crystals with low dislocation densities (B.K. Tanner, 1972; H. Fehmer, W. Uelhoff, 1972; C.H. Sworn,

T.E. Brown, 1972; M. Kuriyama, J.G. Early, H.E. Burdette, 1972, 1973, 1974a, 1974b). Several of the authors have cited the thermal stresses applied by the mold in the Bridgeman technique for its inherently poor quality crystals. The freely supported crystal grown with the Czochralski technique has been found to be dislocation free under optimum growing conditions (B.K. Tanner, 1972; C.H. Sworn, T.E. Brown, 1972).

The study of dislocation images in crystals using X-ray topography has primarily been a program of experiment preceding theory. Dislocation images were first noted as early as 1958 by Lang (1958, 1959a, 1959b). The extension of dynamical and kinematic diffraction theories to crystals with "localized" defects was established in the mid 1960's (D. Polder, P. Penning, 1964; A. Authier, 1966; F. Balibar, A. Authier, 1967) for transmission topography and as recently as 1973 (T. Bedyńska, 1973) for the Berg-Barrett case. The present paper is concerned less with the details of the observed image than with the conditions under which an image is observable. The orientation of the dislocation in the crystal, its corresponding strain field, and the effects of nearby defects can be evaluated through a combination of several X-ray geometries if the dislocations lie within the range of depth observations of the X-ray techniques.

The depth of dislocations below the specimen surface may be determined from stereo pairs of X-ray topographs, as first proposed by Lang (1959a, 1959b). Lang, using what was later

to be called Lang transmission topography, proposed a stereo pair of topographs, hkl and $\bar{h}\bar{k}\bar{l}$, with a stereo angle of $2\theta_B$, where θ_B is the Bragg angle for the reflection. Vreeland (1976) used two geometries of stereo pairs to determine apparent and actual depths of basal dislocations below a (0001) surface in zinc using Berg-Barrett topography. The complementary stereo pair hkl and $\bar{h}\bar{k}$l, where the crystal has been rotated 180° about its axis between topographs, can be used in some cases for Berg-Barrett topography, as in zinc (T. Vreeland, Jr., 1976). In copper, for a (111) surface of the crystal, the choice of 120° rotated reflections hkl, klh, and lhk, loses full complementary stereo, but these reflections can be used both for stereo and for extinction topographs. If one defines a zero-layer topograph as one in which the incident and diffracted X-ray beams, the perpendicular to the reflecting planes, and the perpendicular to the specimen surface are coplanar, then a second available method of stereo topography can be described as obtaining asymmetric topographs which are taken $\pm\alpha°$ off zero-layer along the Bragg cone (K. Haruta, 1965). The present paper extends Vreeland's work (1976) to dislocation images in copper, and to stereo observations in Borrmann transmission topographs.

All present imaging theories are based, at least in part, on Takagi's equations for the wave function of X-rays

(using Maxwell's equations) or electrons (using Schroedinger's equation) in a periodic crystal (S. Takagi, 1962). A large portion of the computations covers perfect crystals of slightly strained crystals (D. Polder, P. Penning, 1964; B. Roessler, R. W. Armstrong, 1968; S. Takagi, 1969; T. Saka, T. Katagawa, N. Kato, 1972a, 1972b, 1973). Appendix A gives some of the details of the much more complex problem of a dislocation in the crystal.

II. EXPERIMENTAL METHODS

The procedures employed to obtain three dimensional information on dislocations in copper in the present investigation may be outlined as follows:

1. Copper single crystals with low dislocation density were grown using a modified Czochralski technique.
2. Specimens in the form of right circular cylinders with their axes parallel to the [111] direction were machined from the as-grown crystals by electrochemical means and subsequently annealed.
3. A square grid pattern of gold dots was evaporated onto one of the end surfaces of the specimens.
4. Fresh dislocations were produced in the specimen by scratching an end surface with a quartz whisker or razor blade.
5. X-ray topographs were taken and enlarged negative prints were obtained.
6. Distortion of the topographs due to the X-ray and film geometry was removed by suitable image processing.
7. Individual dislocation depths were obtained from each set of stereo topographs.

Crystal Growth

The growth of high purity (99.999 percent) copper single crystals essentially follows the procedures of several authors

(B.K. Tanner, 1972; C.H. Sworn, T.E. Brown, 1972). The Czochralski technique was modified for no rotation of the crucible or the copper melt. The seed and crystal were rotated at 2 revolutions per minute, and the growth rate was approximately 1 cm per hour. An axial temperature gradient of less than 2°C/cm and fluctuations in temperature of less than ¼°C were maintained to grow crystals about 2 cm in diameter by 10 cm in length. Figures 1a and 1b show the effects of slight fluctuations in temperature on the diameter of the crystal. The crystals were grown from [111] oriented seeds and, therefore, were all oriented with their cylindrical axis within 5° of the [111] direction. The resulting dislocation densities, as observed by etch pits on a polished (111) surface, were 10^2 to 10^3 dislocations cm per cm^3.

A more complete description of the growth process is included in Appendix B.

Specimen Preparation

Specimens for X-ray topographic experimentation were machined from the as-grown crystals by electrochemical methods so that very few dislocations were introduced during the machining process. Acid sawing and electrochemical polishing of cylinder surfaces and oriented flat ends of right circular cylinders were effected by using a South Bay Technology solvent wire saw and model 452 lathing instrument. Specimens

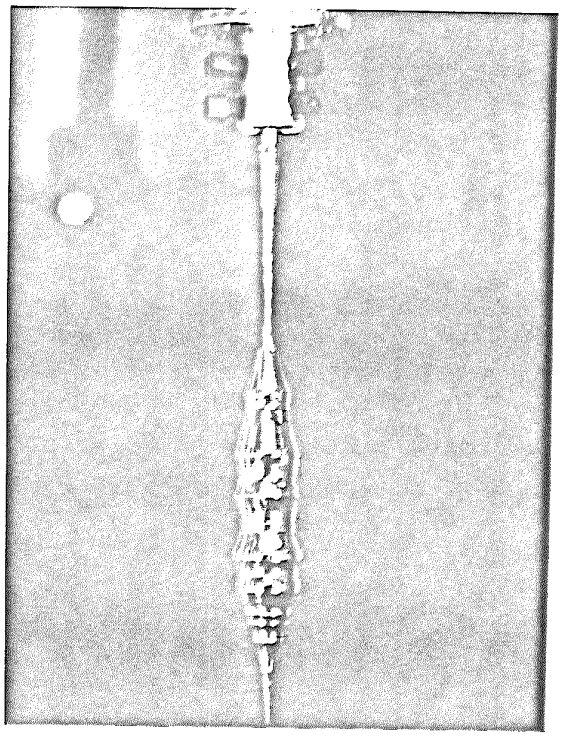

(a)

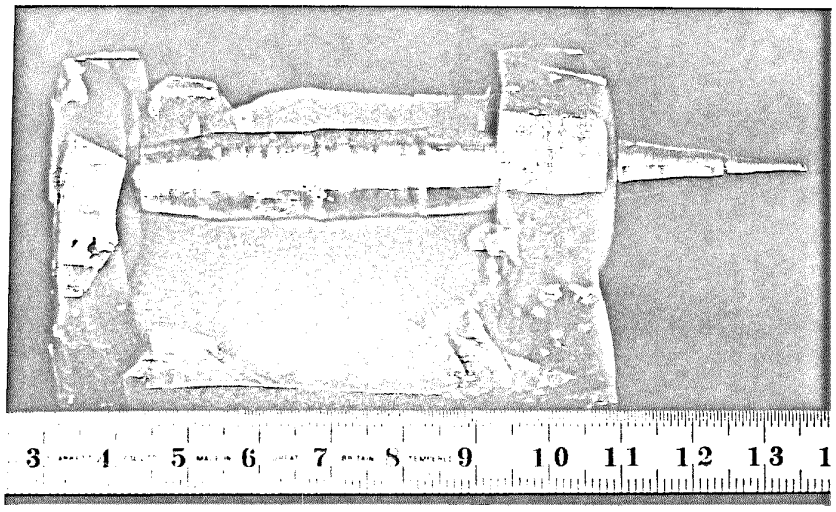

(b)

Figure 1. Copper crystals grown under poor (a) and optimum (b) temperature conditions. The crystal in (a) is still attached to the seed, while the crystal in (b) is imbedded in a wax support and ready for machining.

used exclusively for Berg-Barrett topography were 1.0 to 2.0 cm in diameter by 0.5 to 2.54 cm long. Test specimens which were used both in Borrmann transmission topography as well as Berg-Barrett topography were machined into disks approximately 1.0 cm in diameter by 0.3mm thick. All crystals studied in this work were oriented within 0.1° of (111) surfaces.

The machined test specimens were annealed for two weeks at 1050°C. in an argon atmosphere on a support of high purity graphite. The heating and cooling rates were less than 2° per minute to minimize thermal shock stress. This treatment removed near surface dislocations. The resulting dislocation density observed by using Livingston's etch (J.D. Livingston, 1961), which included dislocations introduced during maching and probably some of the "grown-in" dislocations as well, fell between 10^2 and 10^3 dislocation pits per cm^2 on the (111) surface. The true total density (total length of dislocation line per unit volume) may be larger because the X-ray topographs show long dislocations which do not intersect the etched (111) surface. These were probably Cottrell-Lomer lock dislocations as have been observed by Kuriyama, Early, and Burdette (1974a) under similar conditions of crystal preparation.

Surface Reference Pattern

The determination of the depths of dislocations beneath

the surface of the specimens from stereo pairs of X-ray topographs was facilitated by placing a regular pattern of gold dots on the surfaces by vapor deposition through an aluminum mask. Each gold dot was 40μm in diameter and from 0.1 to 0.5μm thick, while the spacing of the dots in the square grid was about 150μm. The images of the gold dots in the topographs were intended to define the position of the specimen surface. The results, presented below, show, however, that the images of the gold dots actually appear to lie below the specimen surface. Nevertheless, a suitable correction for this effect was found so that the gold dot pattern served the intended purpose.

Introduction of Fresh Dislocations

Jassby and Vreeland (1970) found that scratching along the $[1\bar{1}0]$ direction on the (111) surface of copper produces dislocations parallel to the scratch with Burgers vectors $\frac{1}{2}[101]$ and $\frac{1}{2}[0\bar{1}1]$. All test specimens in the present investigation were scratched along each of the three <110> directions lying in the specimen surface. The scratches were made using quartz whiskers 12 to 100 μm in diameter with loads from 25 to 500 mg. Some scratches were also made using a pointed razor blade. The near surface dislocations found by Jassby and Vreeland (1970) were not observed in the present investigation due to the apparent cross slip of the dislocations to the surface. Fresh dislocations which were not

parallel to the scratches and some deeper dislocations parallel to the scratches were, however, generated by the scratching technique and were observed in the X-ray topographs.

Details on the scratching technique can be found in Pope (1967) and in Jassby and Vreeland (1970).

X-ray Topography

Four different stereo geometries were used to obtain information on the depths of dislocations in the (111) oriented copper specimens. The four methods can be defined as Berg-Barrett extinction topography, asymmetric Berg-Barrett topography, Borrmann diffracted-transmitted beam stereo topography, and asymmetric Borrmann topography. A description of each method and its adaption to the present (111) copper specimens follows.

The Berg-Barrett reflection technique for observing the copper crystals (Figure 2) imposed conditions on α_o, the grazing angle of the incident X-ray beam, and β_o, the angle between the reflected beam and the surface normal, for optimum results. With a narrow incident X-ray beam, approximately 3.0 mm wide, α_o must be small enough to illuminate the entire crystalline surface and yet not too small that the depth of penetration of the X-rays into the crystal is very shallow. The factor $(\beta_o - \alpha_o)$ and β_o itself should both be small to reduce the distortion of the image obtained by the

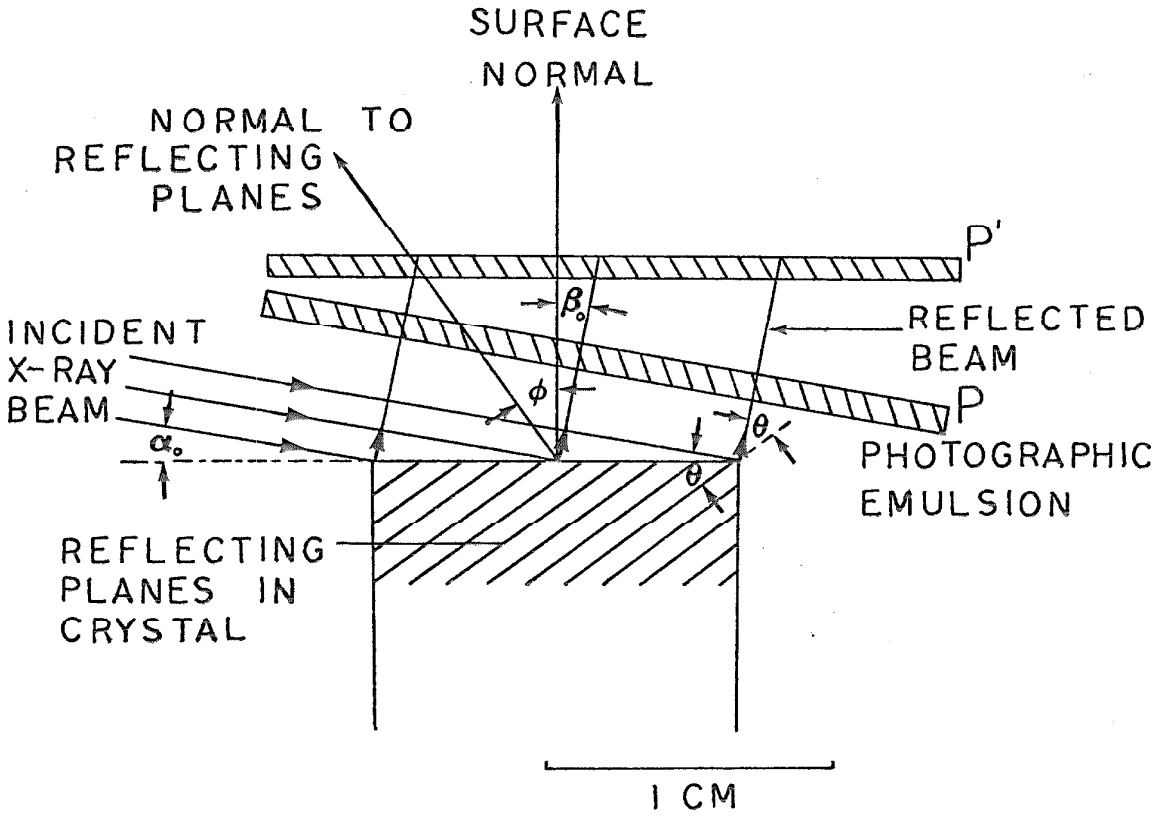

Figure 2. Schematic of geometry for Berg-Barrett topography showing the normal position for the photographic emulsion, P, and the equivalent position for image processed topographs, P'.

photographic emulsion which is set parallel to the incident X-ray beam instead of parallel to the specimen surface. Based on these considerations, the reflections used on the (111) oriented copper specimens with the characteristic cobalt K_α radiation, with a characteristic wave length equal to 1.7902Å, were the 220 type reflections.

Using a different set of (220) reflecting planes for each Berg-Barrett topograph provided information for both stereo measurements and information on the Burgers vectors of dislocations. The stereo angle for a "zero-layer" 220 and 202 pair, in which the incident and diffracted X-ray beam directions, B_oO and $O\alpha$ (or $O\beta$) in figure 3, and the normal to the specimen surface, OH, are coplanar, is $\alpha O\beta$. In the present work, this stereo angle was 19.38°. One criterion for observing dislocations in a crystal is that the Burgers vector, $\vec{b}$, of the dislocation and the normal to the reflecting planes, $\vec{g}$, are not mutually perpendicular. Otherwise the dislocation is not observed or extincted. Therefore, for dislocations with $\frac{1}{2}\langle 1\bar{1}0\rangle$ type Burgers vectors in the (111) plane, the Burgers vectors were determined by taking the three 220 type extinction topographs.

Figure 3 also shows the geometry used for asymmetric Berg-Barrett topography. The specimen was rolled off zero layer about the [111] axis so that the X-ray path followed was B_1OC_1 in one topograph and B_2OC_2 in a second topograph.

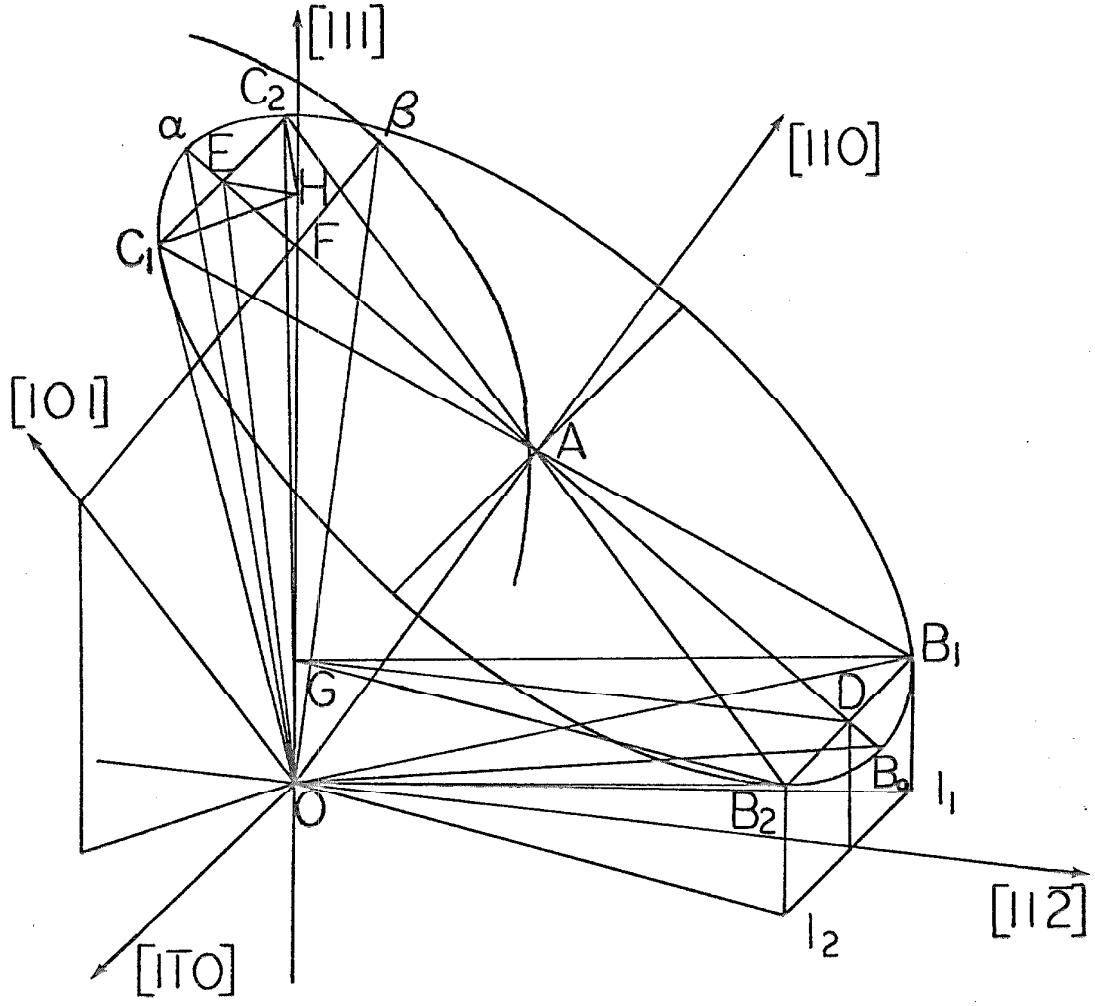

Figure 3. Geometry for Bragg reflection in Berg-Barrett topography for a (220) reflecting plane off a (111) surface of copper. A portion of a second 202 Bragg cone is shown passing through β. The X-rays enter the specimen along the path BO, and exit along the corresponding path OC.

The resulting stereo angle is C_1OC_2, and for the (111) copper specimens, this was 39.1°, when the crystal was rotated ±20° about the surface normal.

Appendix D gives a clear account of the calculations required to obtain these stereo angles from the X-ray and crystal geometry.

For Borrmann transmission topography, on a (111) crystal, a $2\bar{2}0$ reflection was used primarily for its large interplanar spacing and the fact that the anomalous absorption is perpencicular to the specimen surfaces. Figures 4a and 4b show the geometry of the Borrmann topographs. The incident X-ray beam, B_oO in Figure 4a, is channeled along the $(2\bar{2}0)$ planes and splits near the exit surface into the diffracted beam $O\alpha$ and the transmitted beam $O\beta$. Setting the photographic plate parallel to the specimen surface, both the diffracted and transmitted X-ray topographs were obtained. The effective stereo angle was $\alpha O\beta$, twice the Bragg angle, or 74.12° using copper K_{α_1} radiation, with a characteristic wave length equal to 1.5405Å. Figure 4b shows that rotation about the normal to the reflecting planes to the non-"zero layer" or asymmetric X-ray directions B_1OC_1 and B_2OC_2 provides a stereo angle C_1OC_2. Only the diffracted beam image was obtained for these topographs since no further information could be obtained from both diffracted and transmitted X-ray topographs. By rotating about the $[1\bar{1}0]$ direction ±10° the resulting stereo

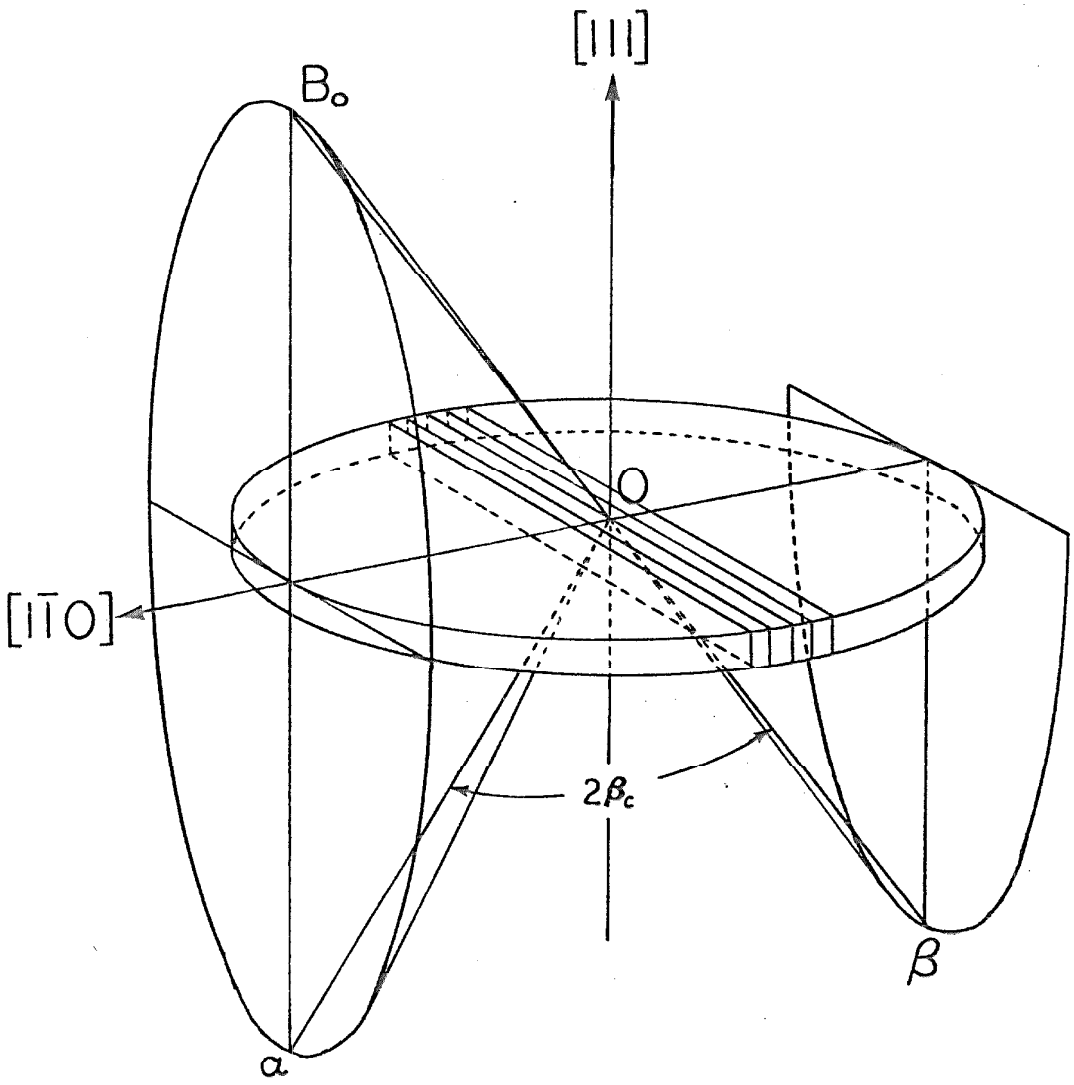

Figure 4a. Schematic of diffracted-transmitted Borrmann topography for a $2\bar{2}0$ reflection off a (111) oriented copper specimen. The incident wave vector is B_oO and the diffracted beam and transmitted beam directions are $O\alpha$ and $O\beta$, respectively.

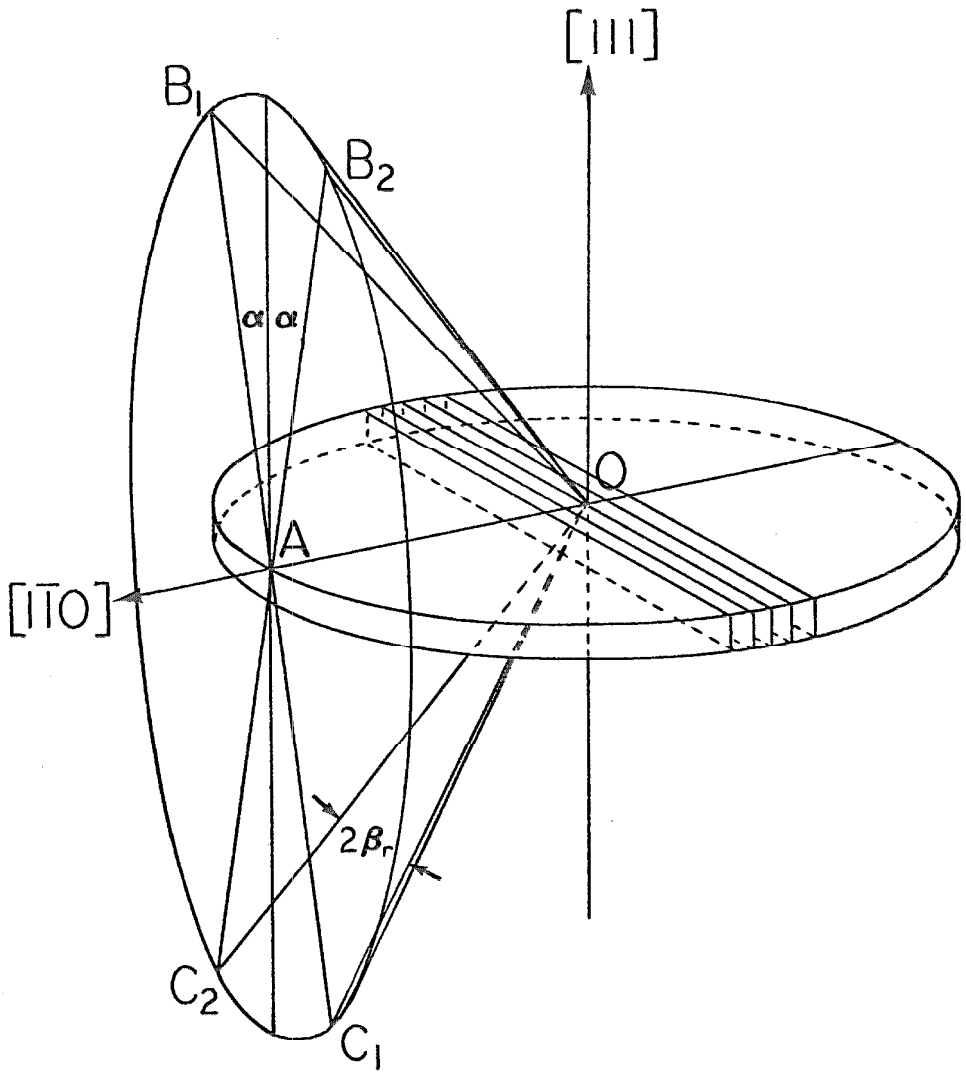

Figure 4b. Schematic of asymmetric Borrmann topography for obtaining a stereo pair of topographs. The specimen is rolled $\pm\alpha°$ from zero layer about the $[1\bar{1}0]$ direction. The resulting X-ray paths are B_1OC_1 and B_2OC_2 with a stereo angle $2\beta_r$.

angle was 15.93°.

Topographs, Printing, and Image Processing

All Berg-Barrett topographs were taken on Kodak High Resolution Plates (HRP) with an emulsion thickness of approximately 5μm. An iron foil 0.1 mm thick was placed in front of the emulsion to reduce the background copper fluorescence intensity with respect to the diffracted cobalt K_α radiation. Exposure times were 10 hours with the X-ray tube set at 40 KV with 7mA current.

Due to the low intensities of the Borrmann transmission X-rays, the Borrmann topographs were taken on Ilford L-4 plates with a 50μm emulsion thickness. For crystals approximately 0.3mm thick, with the copper X-ray tube set at 40kV with 25 mA current, exposure times varied from 40 to 100 hours. No filters were necessary, since the Borrmann effect in the specimen "filtered" all X-rays except the characteristic copper K_{α_1} by kinematic absorption.

Since all the specimens X-ray images were the same size as the specimens it was necessary to magnify the topographs. The topographs were enlarged by a linear factor of 20 onto both positive and negative prints from which the stereo data was obtained.

In the Berg-Barrett method, Figure 2, it is inconvenient to place the plate parallel to the crystal surface (J.B. Newkirk, 1959; Turner, Vreeland, Pope, 1968). To increase resolution,

the photographic emulsion was placed parallel to the incoming X-ray beam as close to the crystal as possible. For some stereo topographs this results in a distortion which is difficult to accomodate by the observer. Specifically, as in Figure 5, the asymmetric Berg-Barrett topographs required processing before data could be obtained. The reference grid of gold dot images was matched to a magnified print of the original aluminum mask for each topograph by the Computer Processing Division of the Jet Propulsion Laboratory. The resulting sets of stereo topographs were undistorted surface maps comparable to placing the original photographic emulsions at P′ instead of P in Figure 2. The processing method is explained in Vreeland (1976).

Stereo Depth Measurements

The pairs of magnified stereo topographs, properly oriented, were observed using a mirror stereoscope (Hilger and Watts, model 5B-180 with binocular unit and "flying spot" stereometer). The image shifts of the dislocations were measured with respect to the nearest gold dot images. Full stereo observations using both eyes simultaneously and a slightly modified blink system proposed by the author were used. The latter method, in which the observer blinks his eyes to observe the images and the "flying spot" positions on each topograph separately, proved more useful when the pair of topographs were of unequal intensity or quality or

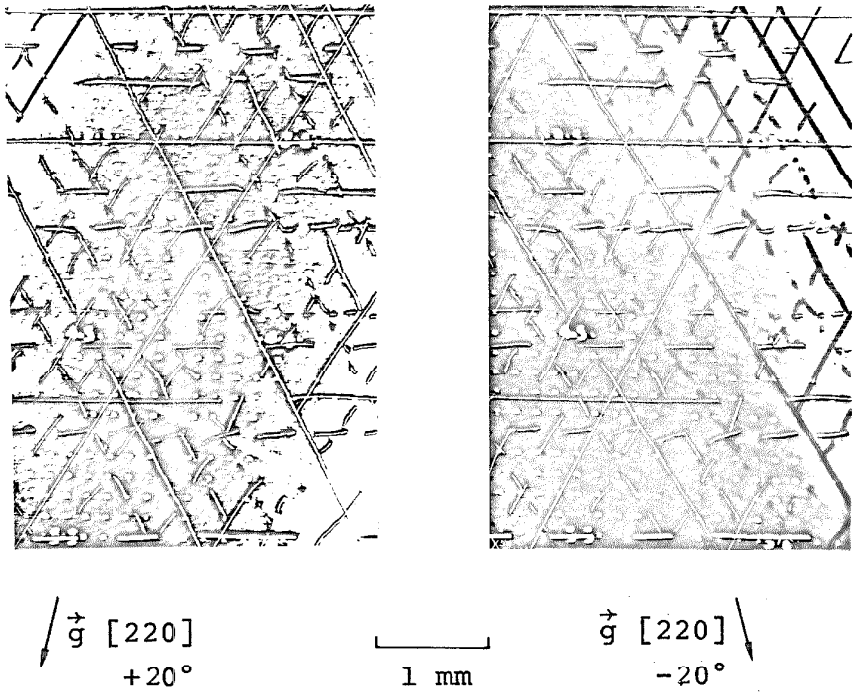

Figure 5. Asymmetric Berg-Barrett stereo pair before image processing.

when the dislocation images were roughly parallel to the stereo direction.

Data on the shifts of dislocation images with respect to the images of the gold dots were reduced to apparent depths of images with the appropriate geometrical information of the topographs and the magnification on the prints, as explained in Vreeland (1976).

III. EXPERIMENTAL RESULTS

Extinction Topography

Figure 6 shows the extinction 'triplet' 220, 202, and 022 topographs. Any two of the three images can be observed for stereo viewing, but the primary information on dislocation structure, namely its Burgers vector, $\vec{b}$, is immediately determined by the extinction criterion. No dislocation image can be observed if $\vec{g}$, the vector perpendicular to the reflecting planes, is perpendicular to the Burgers vector $\vec{b}$. The figures show the projection of $\vec{g}$ in the surface plane as well as the Burgers vector $\vec{b}$ for several regions of dislocations. The dislocations around the gold numbers lie in the (111) plane with Burgers vectors of the $\frac{1}{2}\langle 1\bar{1}0\rangle$ type. The observed Burgers vectors are in agreement with the radial symmetry of the strain field around the gold dot.

Apparent Depth of Gold Dots

A stereo pair of 220, 202 Berg-Barrett topographs are shown in Figure 7. A stereo pair of image processed 220 asymmetrical Berg-Barrett topographs are shown in Figure 8. Quantitative depth measurements on both of these stereo pairs show that the dislocation images are outside the crystal relative to the images of the gold dots! Evidently the images of the gold dots are within the crystal rather than at its surface. It was also noted that on several different

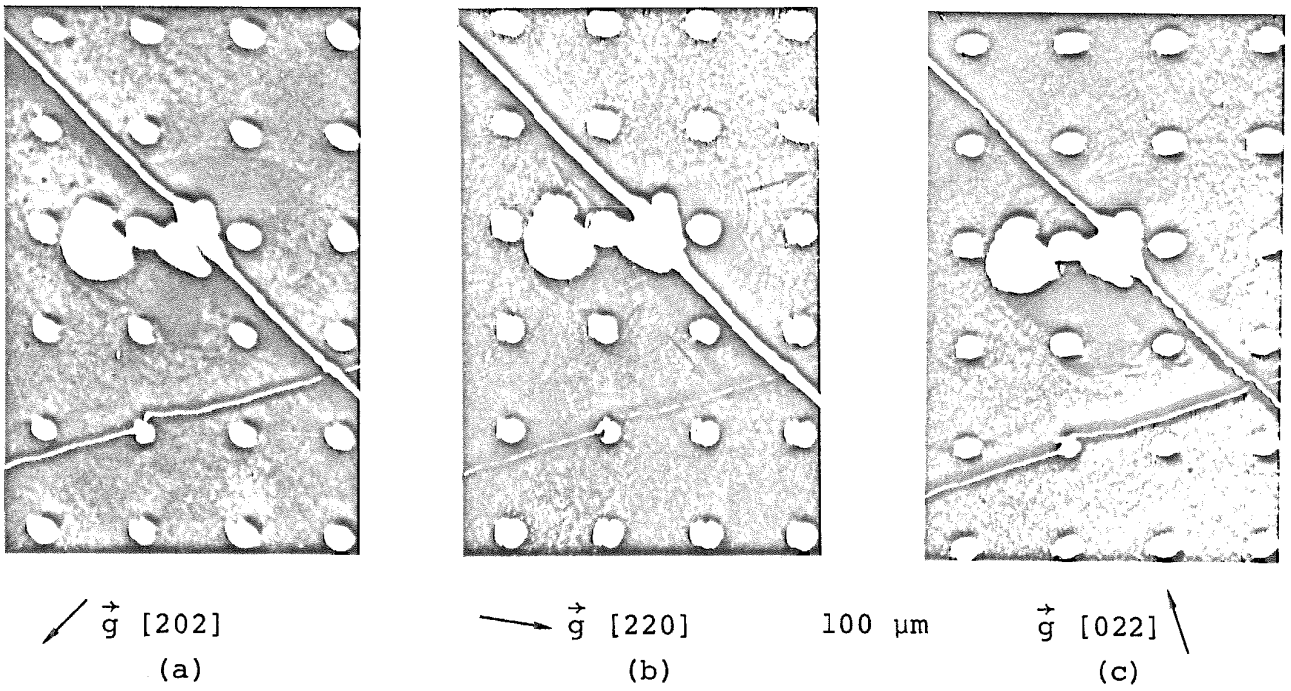

Figure 6. Berg-Barrett extinction triplet showing dislocations near gold grid pattern. The projections in the topograph plane of the normals to the reflecting planes, $\vec{g}$, are noted and some of the directions of the Burgers vectors for the dislocations are marked with arrows in (b).

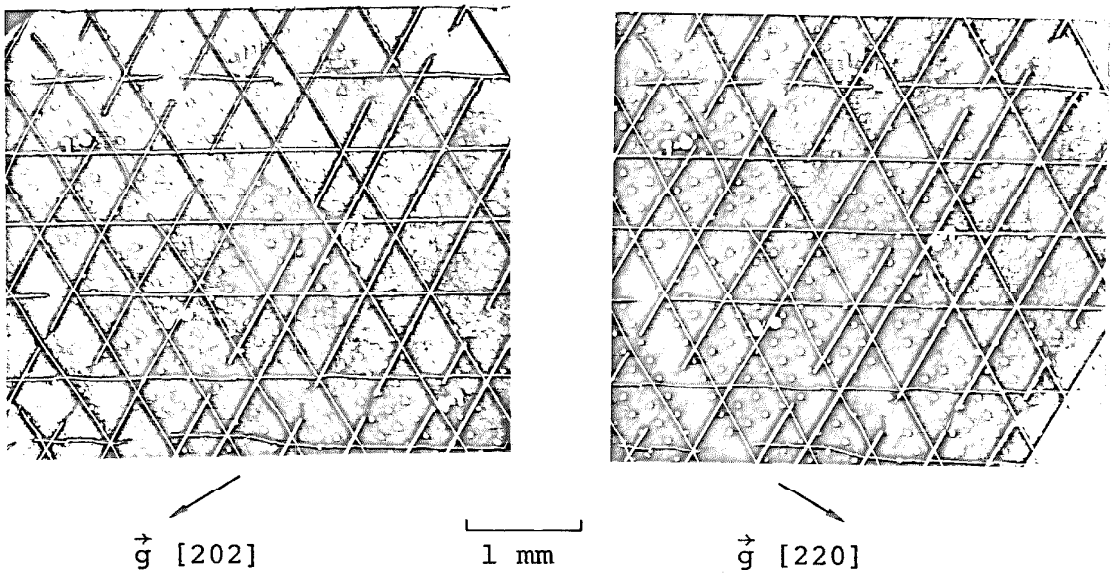

Figure 7. Berg-Barrett extinction stereo topographs to be compared to figure 8.

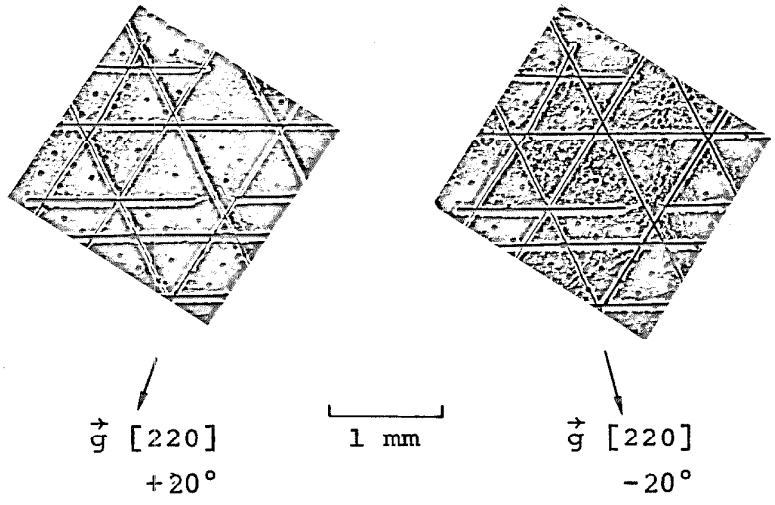

Figure 8. Image processed Berg-Barrett asymmetrical stereo topographs showing the same region of a specimen as Figure 7.

crystals with varying thickness of gold dots, the observed depths of the dislocation images (outside the crystal) relative to the images of the gold dots were larger for the thicker gold dots. A shadowing effect on the incident beam is proposed to resolve this effect.

Although the observer is faced with a light-dark image of each gold dot in the diffracted-transmitted Borrmann topographs, as in Figure 9, quantitative depth measurements on these topographs show that the dislocation images are observed both closer to and further away from the specimen surface with respect to the images of the gold dots. Thus the images of the gold dots are again shifted into the specimen rather than denoting its surface. In this case, however, the shift of the images of the gold dots into the crystal can be explained by a strain field effect instead of a shadow effect.

Observed Dislocation Depths - Berg-Barrett Topography

The apparent depths of dislocation images were determined for both the extinction stereo and the asymmetric stereo pairs. When direct comparison between images of single dislocations was not available, an overall statistical comparison of images from the same specimen was obtained. Table I gives the statistical data for depths of dislocation images with respect to the surface defined by the images of the gold dots in a typical crystal for the two types of Berg-Barrett stereo

Table I. Apparent depth of dislocation images with respect to the images of the gold dots in Berg-Barrett topography.

CRYSTAL NUMBER	REFLECTIONS	OBSERVED MEAN DEPTH, μm	STD DEVIATION, μm	MINIMUM-MAXIMUM READINGS, μm
I	Extinction 220 and 202 reflections	-22.1	6.2	-13.4 to -29.7
	Rolled ±20° from zero layer 220	-4.6	2.0	-2.1 to -7.7
II	Extinction 220 and 202 reflections	-21.3	4.2	not available
	Rolled ±20° from zero layer 220	-4.3	1.3	not available
III	Extinction 220 and 202 reflections	-29.2	13.7	-10.4 to -57.9
	Rolled ±20° from zero layer 220	-3.0	5.4	not available

Note: Negative values of image depths denote images closer to the exit surface of the specimen that the images of the gold dots.

topographs. It should be noted first that the observations are closer to the surface for the larger values of apparent depth with respect to the images of the gold dots. Secondly, no values of dislocation image depths for extinction topographs, h_e, are equal to the corresponding image depths for the asymmetrical (rolled) topographs, h_r. Thus, the term "apparent" depth is used for the observed image depths of the dislocations.

Observed Dislocation Depths - Transmission Topography

Figure 9 shows a stereo pair of Borrmann diffracted-transmitted topographs. Stereo depth measurements in this system were made more difficult due to the light-dark contrasts of the images of the gold dots in the stereo direction. The observer can most easily accomodate light to light matching in the stereo viewer rather than the true light to dark comparison required for the topographs. This results in a constant image shift which must be subtracted from the measured shifts of the dislocation images. The "blink" system of using one eye at a time can also accomodate the problem of the light-dark contour of the gold dot images. Both methods were used to obtain the data in Table II since the computed depths of the two methods were almost identical. The apparent depths of dislocation images fell between 8μm closer to the surface than the images of the gold dots to approximately 12μm deeper into the specimen than the images

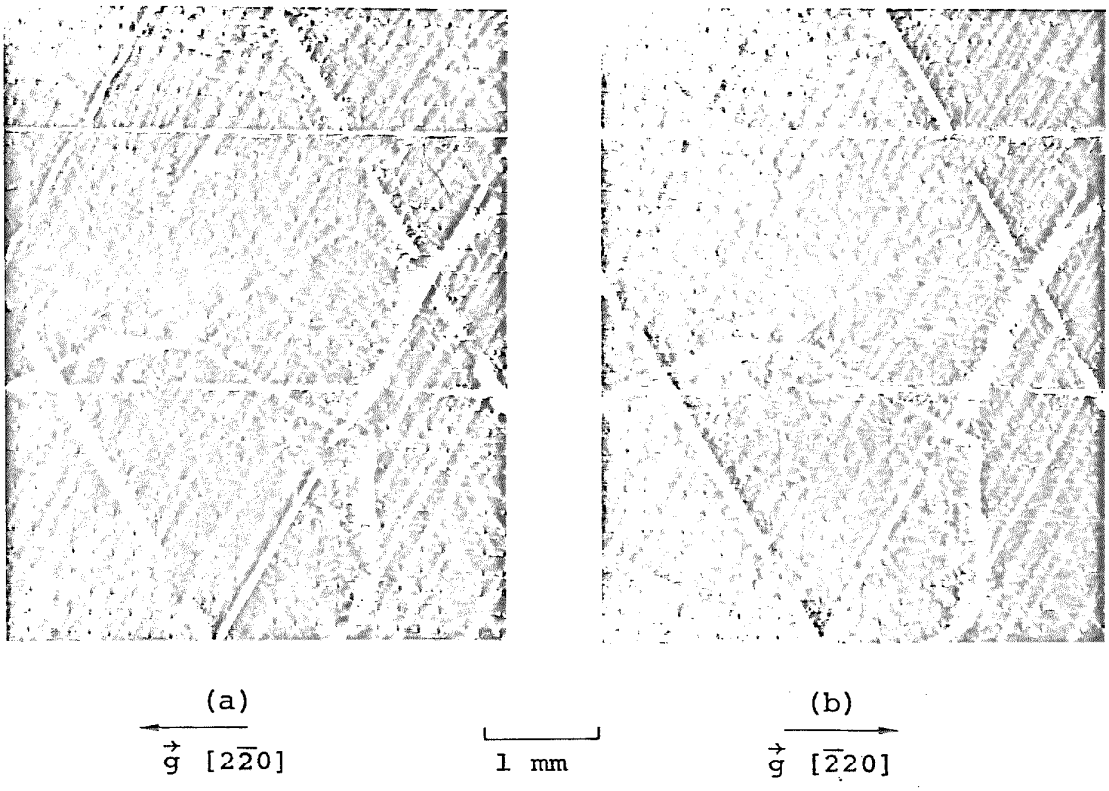

Figure 9. Borrmann diffracted (a) and transmitted (b) beam stereo pair. The light-dark contrast of the images of the gold dots is visible, as well as individual dislocations and small angle boundaries.

Table II. Apparent depth of dislocation images with respect to the images of the gold dots in Borrmann topography.

REFLECTION USED	OBSERVED MEAN DEPTH, μm	STD DEVIATION, μm	MINIMUM-MAXIMUM READINGS, μm
Diffracted-transmitted beam $2\bar{2}0$	-0.3	4.9	-7.6 to 10.6
Diffracted-transmitted beam $2\bar{2}0$ (Cottrell-Lomer dislocations)	3.4	4.6	-4.6 to 12.0
Asymmetric ±10° from zero layer $2\bar{2}0$	152	75	3.5 to 264
Asymmetric ±10° from zero layer $2\bar{2}0$ (Cottrell-Lomer Dislocations)	137	65	30 to 289

Note: Negative values of image depths denote images closer to the exit surface of the specimen that the images of the gold dots.

of the gold dots.

The asymmetric Borrmann stereo topographs yielded apparent dislocation depths from approximately 3.5μm deeper into the specimen than the surface defined by the images of the gold dots to a depth which was, to the accuracy of the data, the entire thickness of the crystal. Table II gives the statistical information on the transmission topography. The Cottrell-Lomer extended dislocations, noted separately, are distinguished in the observations by their wider, more diffuse, images, approximately 100μm versus 2 to 5μm for most other dislocation images, and by their appearance parallel to the (111) specimen surface along the $\langle 1\bar{1}0 \rangle$ directions, as required by the geometry of their structure. No problems due to the light-dark contrasts of the images of the gold dots impaired the asymmetric stereo measurements since the stereo direction was perpendicular to the plane of incidence containing the X-ray beams. Figure 10 shows an unprocessed asymmetrical Borrmann stereo pair which were rolled ±10° from zero layer. It was not considered necessary to image process the prints, although stereo viewing would have been facilitated, since the direction of distortion of the plates was perpendicular to the stereo direction.

Comparison of Berg-Barrett and Borrmann Topography

For the crystals in which it was convenient to observe both Borrmann transmission and Berg-Barrett reflection stereo

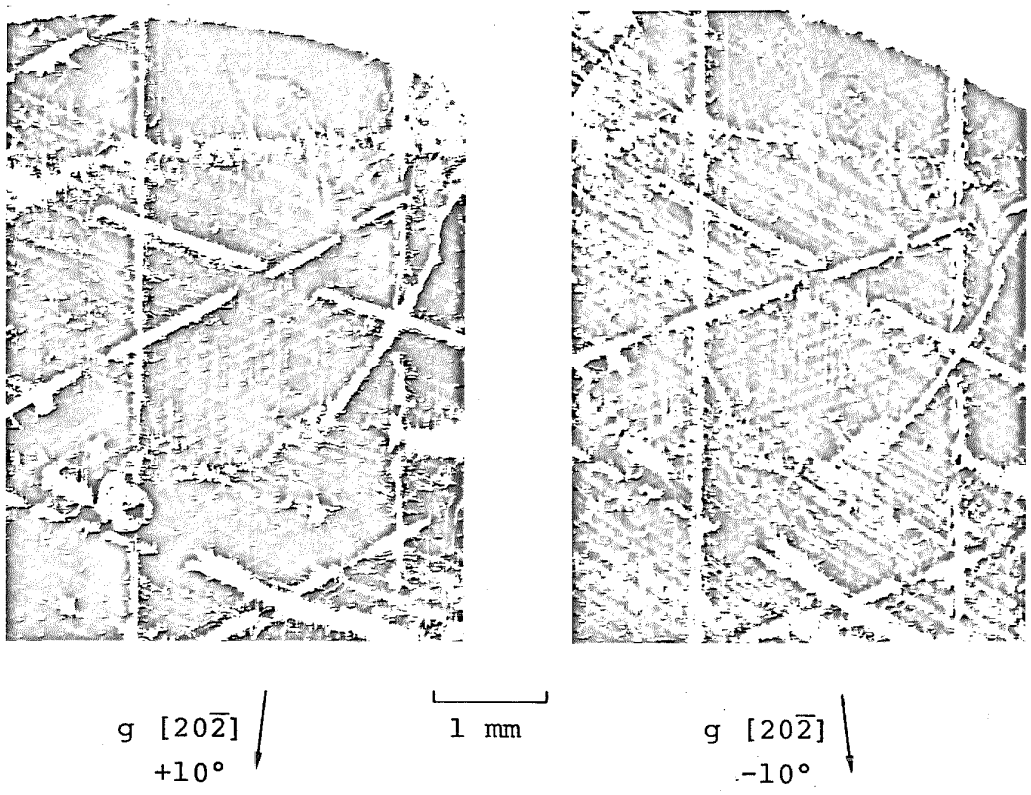

Figure 10. Asymmetric Borrmann stereo topographs taken ±10° from zero layer. Note the large image shifts of the long dislocations (arrow), implying very deep observations.

topographs, no correlation of images existed between the dislocations observed in transmission and those observed in reflection. Whereas the transmission topographs showed many defects including low angle grain boundaries, the reflection topographs are essentially clear of images except very near the scratches. Hence, the range in depth of observation of dislocations in Berg-Barrett topography does not coincide or even overlap with the range of observations in Borrmann topography. Figure 11 shows a pair of topographs explicitly showing the difference in images of specimens using Berg-Barrett and Borrmann topography.

Errors in Observations

Systematic procedures which lead to errors in data were of several types. The fundamental step of stereo measurements was confused by diffuse gold dot images, unresolvable or extincted dislocation images, the photographic plate emulsion thickness, and real distortions in the stereo plates. These problems would all tend to increase the standard deviation of the data. Due to the long period of time between many stereo observations, there is a high probability that some dislocations had moved between topographs, and stereo measurements will be incorrect. One cannot remove these data points from the total data. The long time span also leads one to conclude that dislocation very near the surface (which might be observable in early topographs) may diffuse out of the crystal, leaving a lower density in an observable region.

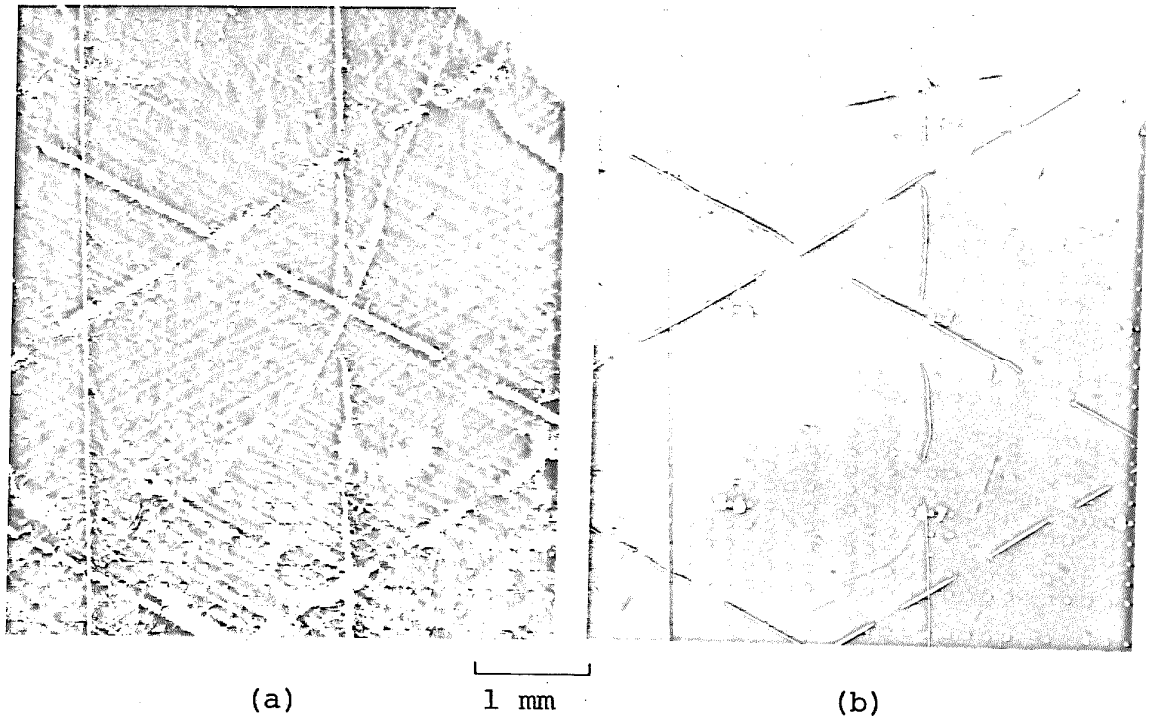

Figure 11. Comparison of Borrmann transmission topograph (a) with Berg-Barrett reflection topograph (b). Small angle boundaries and the deep extended dislocations are observed in the Borrmann topograph. Only dislocations near the scratches are visible in the Berg-Barrett topograph.

IV. DISCUSSION

The data from both Berg-Barrett and Borrmann diffracted-transmitted beam stereo topographs show that the apparent depths of dislocations relative to the gold dots, h, are not equal to the actual depths, H, of the dislocations below the surface. In the Berg-Barrett topographs, nearly all dislocation images are above the gold dot images ($h<0$, the dislocations appear to be "outside" the crystal if the dots are assumed to appear at the surface). In the Borrmann diffracted-transmitted beam topographs, the images of the dislocations were observed both above ($h<0$) and below ($h>0$) the gold dot images. The apparent depths of dislocation images are so different in the Berg-Barrett extinction pairs and the rolled pairs that one is led to assume a relationship between apparent depth and real depth which is a function of the stereo geometry of the topographs. The apparenty arbitrary results can be understood and suitable corrections can be made to obtain the true depths of dislocations below the surfaces of the specimens by considering the mechanisms of image formation in the X-ray topographs, as will be shown below.

Figure 11, which shows a typical Borrmann topograph and a corresponding Berg-Barrett topograph for the same crystal, does not provide any stereo depth information on any images of dislocations, but it does show that the regions of observations in the Borrmann and Berg-Barrett cases do not

overlap significantly. This provides limiting evidence on the maximum real ranges of observation. However, this evidence should only be used to check other data, not as a direct source of data on depths of dislocation images.

Image Formation in Berg-Barrett X-ray Topography

Figure 12 shows a gold dot of finite thickness on the surface of a specimen and the limiting rays of radiation which produce the boundaries of its stereo image on the photographic plates when these images are obtained by a complementary pair of Bragg reflections. This limiting ray geometry shows that the stereo image of the gold dot appears to be inside the specimen at a distance

$$H_o \simeq \frac{t}{\tan \alpha_o \tan \beta_o}$$

from the surface, where t is the thickness of the gold dot, α_o is the grazing angle of the incident beam with respect to the specimen surface and β_o is the angle between the reflected beam and the surface normal (Figure 2). If a factor of $\sin(\psi/2)$, where ψ is the angle between the projections in the surface plane of the reflected beams, multiplies the right hand side of the above equation, then the equation is correct for extinction topographs and rolled topographs as well as for the complementary stereo topographs. Thus

$$H_o \simeq \frac{t}{\tan \alpha_o \tan \beta_o} \sin(\psi/2)$$

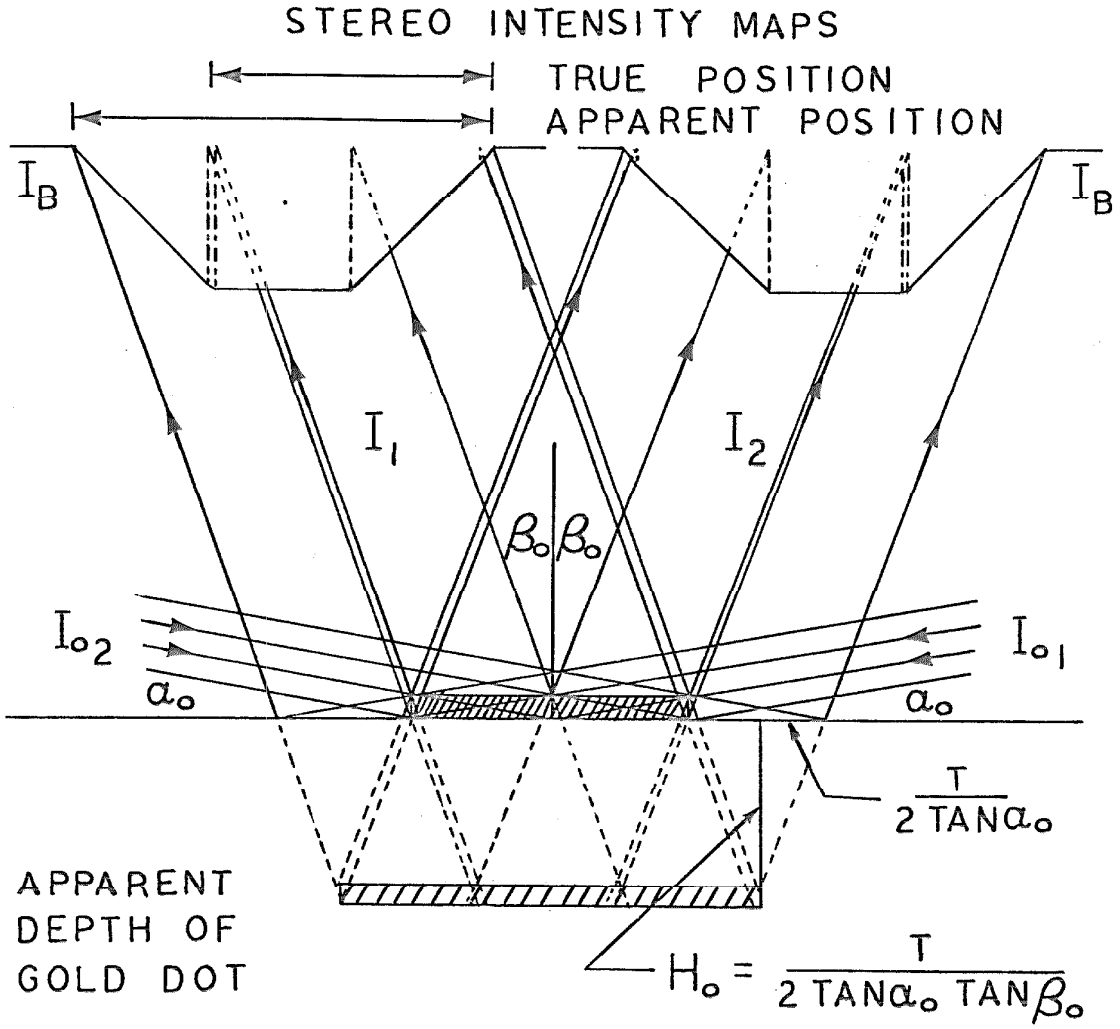

Figure 12. Schematic of complimentary stereo pair of Berg-Barrett topographs showing the apparent depth, H_o, of the image of the gold dot due to the shadowing of the incident beam, I_o.

With $\psi = 180°$, for the complementary pair, this equation reduces to the previous one. With the appropriate values of α_o, β_o, and ψ, and assuming a gold dot thickness of 0.2μm (the range of dot thickness was 0.1μm to 0.5μm), the values of H_o for the extinction and the rolled topographs, can be determined. The results are given by

$$H_{oe} \simeq \frac{0.2}{\tan 9.36° \tan 12.0°} \sin(120°/2) = 5.3\mu m$$

and

$$H_{or} \simeq \frac{0.2}{\tan 11.21° \tan 17.77°} \sin(40°/2) = 1.0\mu m$$

Unless one knows the actual thickness of the gold dots, one cannot determine exactly what actual depths of dislocations are being observed due to the uncertainty in the apparent depth of the images of the gold dots. It was observed, however, that the dislocations in the crystals with thicker (0.5±0.1μm) gold dots did appear at larger apparent depths h, with respect to the images of the gold dots, than those in crystals with thinner (0.1±0.05μm) gold dots, as is expected with the present assumptions. Thus the real depth, H, of the dislocations in the crystal can only be determined to within a constant factor, at best. Therefore, the statistical mean of the data for each crystal is a source of information on the gold dots and not directly on the depths of the dislocations.

The apparent depths of dislocation images are so different in the extinction pairs and the rolled pairs of Berg-Barrett topographs that one is forced to assume a geometrical relationship between apparent depth and real depth. The data are only partly satisfied by the constant factor H_o due to the image shift of the gold dots, as in

$$H_o + h = H$$

where H_o may vary with the geometry. However, the standard deviations of the data for the two types of topographic pairs are also not in agreement as they should be with an equation of the form shown above. The apparent relative depths of dislocations with respect to each other, which are observed through the standard deviations of the data for example, are larger by a factor of approximately 3 in the extinction stereo pairs than the relative depths observed in the corresponding rolled stereo pairs. An exact point-to-point correspondance between individual dislocations observed in both extinction pairs and rolled pairs supported the statistical evidence that there is a greater spread in h_e, the extinction apparent depths, than in h_r, the rolled apparent depths.

An image shift which is a function of depth, as proposed by Vreeland (1976) and explained in Figure 13 for a complementary pair of topographs with channeling along the reflecting planes, is required to satisfy the data on

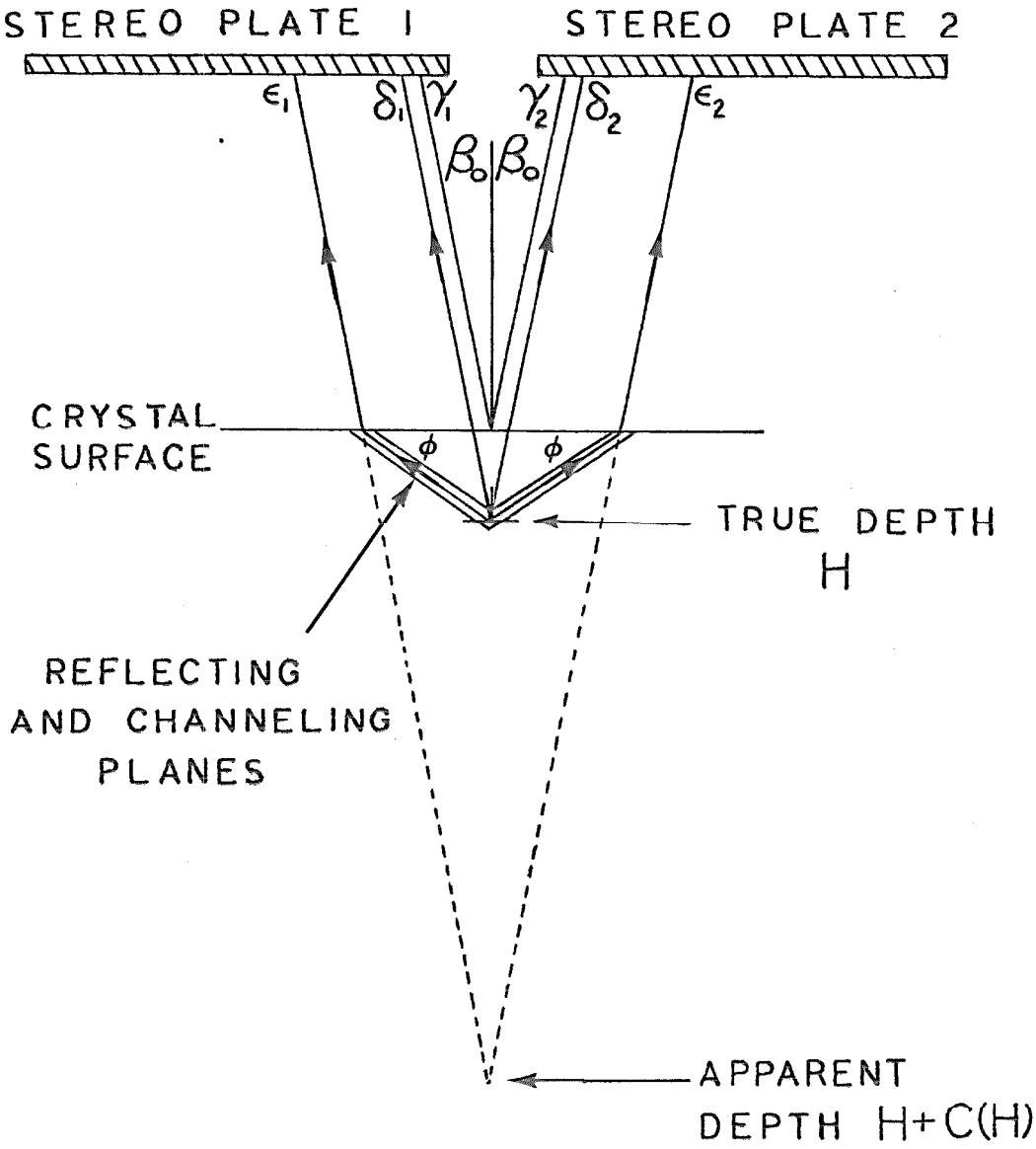

Figure 13. Schematic of shift of dislocation images in "processed" Berg-Barrett stereo pair topographs due to channeling of X-ray information along the reflecting planes. The change in apparent depth, C(H), is a direct function of the reflection geometry.

standard deviations of both extinction and rolled stereo topographs. An equation for the actual depth versus apparent depth would then be of the form

$$H_o + h = H + C(H)$$

where C(H) is a function of the actual depth which is also a function of the stereo geometry. Stereo geometry stipulates the form of C(H) to be

$$C(H) = 2KS\sin\beta$$

where K is a geometrical factor, S is the actual image shift along the surface of the specimen in the incidence plane (containing $\vec{k}$ and the surface normal), and β is the half angle in the surface plane between the exit beams of the two stereo topographs. The factor K can be obtained, as in Vreeland (1976), for both stereo conditions. For extinction stereo the factor is

$$K_e = \cos(\beta_e - \alpha_e)/(2\sin\beta_e) = 2.969$$

and

$$\beta = 60°$$

The corresponding values for the rolled stereo pairs are

$$K_r = \frac{\cos(\beta_r - \alpha_r)\ \cos\beta_r}{\cos\alpha_r\ \sin\beta_r} = 1.408$$

and

$$\beta = 20°$$

The resulting equations are as follows:

$$H_{o_e} + h_e = H + 5.142S_e(H)$$

$$H_{o_r} + h_r = H + 0.963S_r(H)$$

It should again be noted that h_e and h_r are negative in this form of the equation so that as the absolute value of h increases, H decreases.

No further information can be obtained on the accuracy of the theoretical equation unless one assumes a form for the image shift, S(H). It is possible to assume that the image shifts S_e and S_r are functions only of the geometry of the crystallographic planes of reflection and not of the specific rolled angle on the Bragg cone. For this case, therefore,

$$S_e = S_r = S(H)$$

is assumed. Channeling of the information returning from the defect below the crystal surface along the planes of reflection, as in Figure 13, can accomodate the data with the fewest assumptions. A linear form for the image shift

$$S(H) = A + BH$$

where A and B are constants for a given set of crystallographic planes, is a logical step if one assumes some channeling along the planes. A given depth (which may be zero), above which the absorption of non-channeled X-rays is low, provides a cut-off on the full channeling of all

information along the planes.

Without a more accurate value on the gold dot thickness than is available in the present research, the errors in evaluating A are too great, but B should be determinable from the relative standard deviations. If the equations are adapted to measure relative apparent and real depths, they become

$$\Delta h_e = \Delta H + 5.142B\Delta H = \Delta H(1 + 5.142B)$$

and

$$\Delta h_r = \Delta H + 0.963B\Delta H = \Delta H(1 + 0.963B)$$

To satisfy the data on standard deviations and direct point-to-point data, the following conditions must be met (from Table I):

$$\frac{\Delta h_e}{\Delta h_r} = 3 \pm 0.5$$

giving

$$\frac{1 + 5.142B}{1 + 0.963B} \simeq 3$$

and

$$B = 0.89 \pm 0.5$$

Theoretically, the limitations on B are zero for no channeling, and 0.96 to 1.1 for full channeling along the (110) planes, as in Figure 13.

If one proceeds using the computed value of B, one obtains the actual depth range ΔH from either set of data,

the extinction or the rolled stereo topographs. The real depth range observable under Berg-Barrett techniques used in this work varied from a minimum of 0.5μm to a maximum of 2.1μm, based on the present theory. This is consistant with the mass absorption depth of 1.95μm, the depth at which the absorption of the incident beam is large and, therefore, the depth below which the intensity of the reflected beam is effectively zero.

Image Formation in Borrmann X-ray Topography

Figure 14 shows a gold dot grown epitaxially onto the surface of a specimen, the associated strain region within the copper crystal generated by the atomic mismatch of the two species, and the limiting rays of radiation which produce the boundaries of its stereo image on the photographic plates for the diffracted and transmitted beams of a Borrmann topograph. As in the Berg-Barrett case, this limiting ray geometry shows that the stereo image of the gold dot appears to be inside the specimen at a distance

$$H_o \simeq \frac{R_o\ (1-\cos\ \theta_B)}{2\sin\ \theta_B}$$

where R_o is the radius assumed for the hemispherical strain field within which the Borrmann Bloch wave (Appendix A) is decoupled into a diffracted and a transmitted beam. With

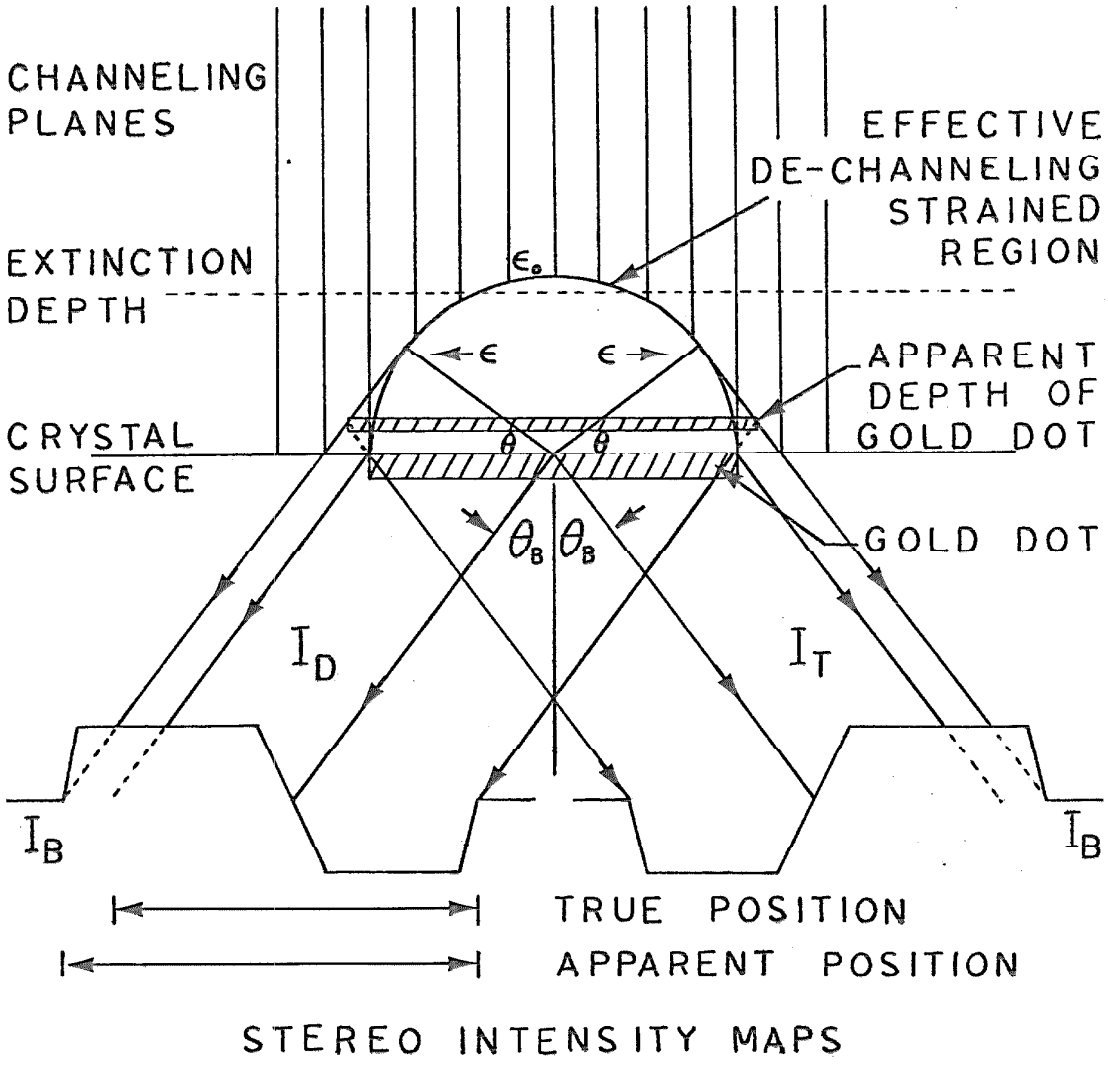

Figure 14. Schematic of Borrmann diffracted beam - transmitted beam stereo pair showing the apparent depth of the image of the gold dot due to a hemispherical strain field within the crystal around the gold dot.

$$R_o \simeq 20\mu m$$

and

$$\Theta_B = 37.06°$$

the value for H_o is 3.5μm. Thus, based on the same theoretical assumptions as in the Berg-Barrett method, the actual stereo depth and the apparent depth may be related by the equation

$$H_o + h = H$$

The overall apparent depths of the dislocation images measured with respect to the images of the gold dots ranged from -8μm (outside the crystal if one assumes the gold dots define the surface) to 12μm (inside the crystal with respect to the gold dot "surface"). The correction factor of H_o, 3.5μm, resets the observed range to -4.5 to +15.5μm. The shape of the strain field associated with each gold dot, the size of the effective decoupling region, and the errors in determining a "zero" surface of the light-to-dark images of dots can easily accomodate the still negative depth measurements. The overall range of observations, approximately 20μm, is in reasonable agreement with the absorption depth of 17μm, as in the Berg-Barrett case.

Channeling of the information from dislocations down the $(2\bar{2}0)$ planes instead of in the $\vec{k}$ and $\vec{k}'$ X-ray directions, would reduce the values of measured depths. The relative values of h would then be less than H, the real values of

the depths. The present data provides no information on this possibile image shift except that it is a relatively small effect since the range of apparent depths is very close in magnitude to the absorption depth.

As explained in Appencix C and in Figure 14, the apparent depth of the gold dot images in the Borrmann case is a function of the strain fields along the X-ray directions $\vec{k}$ and $\vec{k}'$. Therefore, for the asymmetrical stereo topographs in which the stereo direction is ±80° from the X-ray directions of the two topographs, the image shift of the gold dots yields a shift in apparent depth of only

$$H_o \simeq (3.5\mu m)\sin 10°$$
$$\simeq 0.6\mu m$$

where the 3.5μm is obtained from the previous section.

The dislocation images in the asymmetrical case are distributed evenly in depths from 3.5μm below the surface defined by the images of the gold dots to maximum values that are within 5% of the total thickness of the crystal, 270μm. The minimum depths of observation, 3.5μm, may simply be the result of too narrow an image (Narasimhan and Roessler, a, b), or the result of diffusion of dislocations that were near the surface out of the specimen over the approximately 35 day period of obtaining data. The channeling of the information from the dislocation along the $(2\bar{2}0)$ reflection planes causes no additional shift of the

image in the stereo direction other than the depth information directly, since all information is being channeled by the same planes. Thus, based on the same theoretical assumptions as in the Berg-Barrett method, the actual stereo depth and the apparent depth of dislocations are related by the equation

$$H_o + h = H$$

which, to the accuracy of the available data, shows that the observed depths in the asymmetrical Borrmann topographs are equal to the actual depths of the dislocations in the specimen.

Summary and Further Research

The following conclusions are direct results of the present research concerning stereo depth measurements:

1. The apparent depth of dislocations observed in X-ray stereo topography depends on the geometry used.
2. It is essential to assume an image shift which is a function of depth to satisfy the data.
3. Two or more sets of stereo topographs taken under different stereo conditions can provide information on image shifts and the actual depths.
4. A linear functional form for the image shift versus depth is supported by the data and is in direct agreement with the theory of planar channeling of information along the reflecting planes.
5. The actual observed depths in Berg-Barrett techniques are approximately 0.5 to 1.5 times the depth for which the mass absorption coefficient, μt, is equal to unity.
6. Stereo transmission topographs can provide depth information on dislocations under two different geometries.
7. The asymmetrical stereo measurments use the available anomalous Borrmann topography to obtain exact stereo depths of dislocations. No assumption of image shift is needed to obtain true depths from

the data.

8. The kinematic diffraction-transmission stereo method is a new method by which depth information can be obtained for dislocations near the surface of a specimen. Comparable to the Berg-Barrett method, the real observed depths are of the order of the absorption depth for this kinematic stereo effect.
9. An asymmetric shift of the dislocation image away from the core of the dislocation would produce an apparent depth correction which has not been considered in this work.

Some proposed means of explaining remaining questions and the directions in which future research should be led are described in the following statements:

1. With the available transmission topography for thin crystals, and noting the very shallow observation depths in Berg-Barrett topography, the future observations of dislocations in copper should, under most conditions, be made using one of the two transmission stereo methods.
2. The linear form for image shift as a function of actual depth assumed in this paper may be confirmed by using other available reflections with different geometries, specifically the surface reflections where the shift should be infinite. Stereo topographs

using the surface reflection with varying stereo angles should be taken and evaluated. Dislocations have been observed using the surface reflection, so the image shift is not infinite, but no stereo topographs have been obtained, to the author's knowledge.

3. No dislocations were observed in both transmission and reflection topographs, when this information was available for the same crystal. This fact has been used to set restrictions on observation depths. However it would be more useful to have dislocation images to compare in both cases. Narasimhan and Roessler (a) have observed dislocations closer to the exit surface in the transmission case using an intermediate line focus method to obtain the asymmetric Borrmann stereo topographs. The increase in the image thickness of dislocations near the surface may provide sufficiently shallow observations of dislocations to compare directly to the Berg-Barrett topograph images.
4. Image processing, no matter how effective, will lose some resolution. It might be necessary to set the film parallel to the crystal surface. The lost resolution due to having the film further away from the crystal may not be as important as having a perfect surface map.

5. It would be very useful, as in Vreeland's (1976) work on basal dislocations in zinc, to have an independent measurement of real depth shifts (as a function of tilt to the surface plane). Unfortunately, in copper, the dislocations are often likely to cross slip out of the surface (111) plane. The sessile dislocations lying along the $\langle 1\bar{1}0 \rangle$ directions with Burgers vectors $1/6\langle 11\bar{2} \rangle$ may provide some valuable information in this direction.

APPENDIX A

Dynamical Theory of X-ray Diffraction

For a perfect crystal with no absorption, the classical solution of the propagation equation, derived from Maxwell's equations, for an X-ray beam travelling through the crystal is fairly straightforward. For example, if ψ represents the induction or the electric displacement at any point in the crystal, then the propagation equation becomes

$$\Delta\psi = \frac{1 + \chi}{c^2} \frac{\partial^2\psi}{\partial t^2} \tag{A-1}$$

where c is the velocity of light in vacuum and χ is the dielectric susceptibility in the medium. If the susceptibility is a constant, the equation is satisfied by the plane wave form

$$\psi = \psi_o \exp\{2\pi i(\upsilon t - \vec{k}\cdot\vec{r})\} \tag{A-2}$$

where

$$|\vec{k}| = k = (\upsilon/c)\sqrt{1 + \chi}$$

with $\sqrt{1 + \chi} = n$, the index of refraction of the material.

A periodic medium in which the susceptibility is a slowly varying function of position is assumed by several authors (Penning and Polder, 1961; Polder and Penning, 1964; Roessler and Armstrong, 1968; Saka, Katagawa and Kato, 1972a, 1972b, 1973; Takagi, 1969; Taupin, 1967) to be of the Fourier expansion form

$$\chi(\vec{r}) = \sum_h \chi_h \exp\{-2\pi i \vec{h}\cdot(\vec{r} - \vec{u})\} \tag{A-3}$$

where $\vec{h}$ is the reciprocal lattice vector, $\vec{u}$ is the vector defining the displacement from normal position of the electronic structure at $\vec{r}$, and χ_h are the Fourier coefficients of expansion.

Following Takagi's (1962) method, one assumes a modified Bloch wave form for the solution

$$\psi(\vec{r}) = \left(\sum_h \psi_h(\vec{r}) \exp\{-2\pi i \vec{K}_h \cdot \vec{r}\} \right) \exp 2\pi i \upsilon t \qquad \text{(A-4)}$$

where

$$\vec{K}_h = \vec{K}_o + \vec{h}$$

with $\vec{K}_o$ equal to the incident X-ray beam in the crystal. The solution to equation A-1, using the expansions A-3 and A-4, is simplified by the assumption that at most only a few waves are excited in the crystal. Takagi (1962) and other authors chose two waves, the incident wave and one diffracted wave, as the basis for the following results. If $\psi(\vec{r})$ can be reduced to the form

$$\psi(\vec{r}) = \exp 2\pi i \upsilon t \{ \psi_o \exp 2\pi i (\vec{K}_o \cdot \vec{r}) + \psi_h \exp 2\pi i (\vec{K}_h \cdot \vec{r}) \} \qquad \text{(A-5)}$$

then the solution of A-1 gives Takagi's equations:

$$\begin{aligned} \frac{\partial \psi_o}{\partial s_o} &= -i\pi k C \chi_{\bar{h}} \psi_h \\ \frac{\partial \psi_h}{\partial s_h} &= -i\pi k C \chi_h \psi_o + 2\pi i \{ k\beta_h - \frac{\partial}{\partial s_h} (\vec{h} \cdot \vec{u}(\vec{r})) \} \psi_h \end{aligned} \qquad \text{(A-6)}$$

where s_o and s_h are unit vectors in the incident and diffracted beam directions, C is a polarization factor which is either unity or $\cos 2\Theta_B$ for the wave function being perpendicular or parallel to the incidence plane, k is the wave number in the material, and β_h is given by

$$\beta_h = \frac{|\vec{K}_h| - |\vec{K}_o|}{k_o}$$

A non-trivial solution of equations A-6 requires that the determinantal equation derived from these equations is satisfied. The resulting intersecting "spheres" in reciprocal space of possible $\vec{K}_o$ and $\vec{K}_h$ vectors is defined as Ewald's surface. For any point on the surface the values of ψ_o and ψ_h can be evaluated from equation A-6.

Although most authors have assumed some absorption in the material, usually by providing an imaginary component to the susceptibility and the wave vectors, the basis for most calculations is a limiting value. Either little or no absorption is assumed or a large absorption is assumed in which the Borrmann anomalous absorption dominates in the calculations. It is not clear to this author that anyone has undertaken the problem of partial mass absorption and partial anomalous absorption in a crystal. It seems apparent that near the exit surface of the specimen in both Berg-Barrett and Borrmann topography, the two absorption effects must be coupled. The essential difference in the two topography

systems is the boundary conditions at the surface.

The solution to equation A-1, using expansion A-3, or equation A-6 is immediately complicated by the addition of a localized strain field, as with a dislocation. First, equation A-1 itself becomes more complicated for a rapidly varying dielectric susceptibility. It becomes

$$\Delta\vec{\psi}(\vec{r}) + \vec{\nabla}X\vec{\nabla}X(\chi(\vec{r})\vec{\psi}(\vec{r})) = \frac{1}{c^2}\frac{\partial^2\vec{\psi}(\vec{r})}{\partial t^2}$$

where $\vec{\psi}(\vec{r})$ is now the vector displacement. Second, given information on the incident beam and any localized strain in the integration region, the solution to equation A-6 must be calculated over the entire grid region shown in Figure 15 in order to obtain the solution for the exit beam. Kuriyama and other authors (Kuriyama, 1967 through 1975; Ashkin and Kuriyama, 1966; Kuriyama and Miyakawa, 1970) have assumed that it is not possible to use Takagi's form for solutions to the wave equations in a crystal which has a localized defect. Kuriyama assumes a fully quantum mechanical form for the system of wave field and crystal electrostatic field, and the integration region of his equations is equal to the regions in Figure 15.

To obtain a solution for any but the simplest problems, it is necessary to use a computer to solve either Takagi's equations or Kuriyama's equations. The natural reference vectors $\vec{s}_o$ and $\vec{s}_h$ yield a coordinate system for the calculations. The solution at each point is a function of the

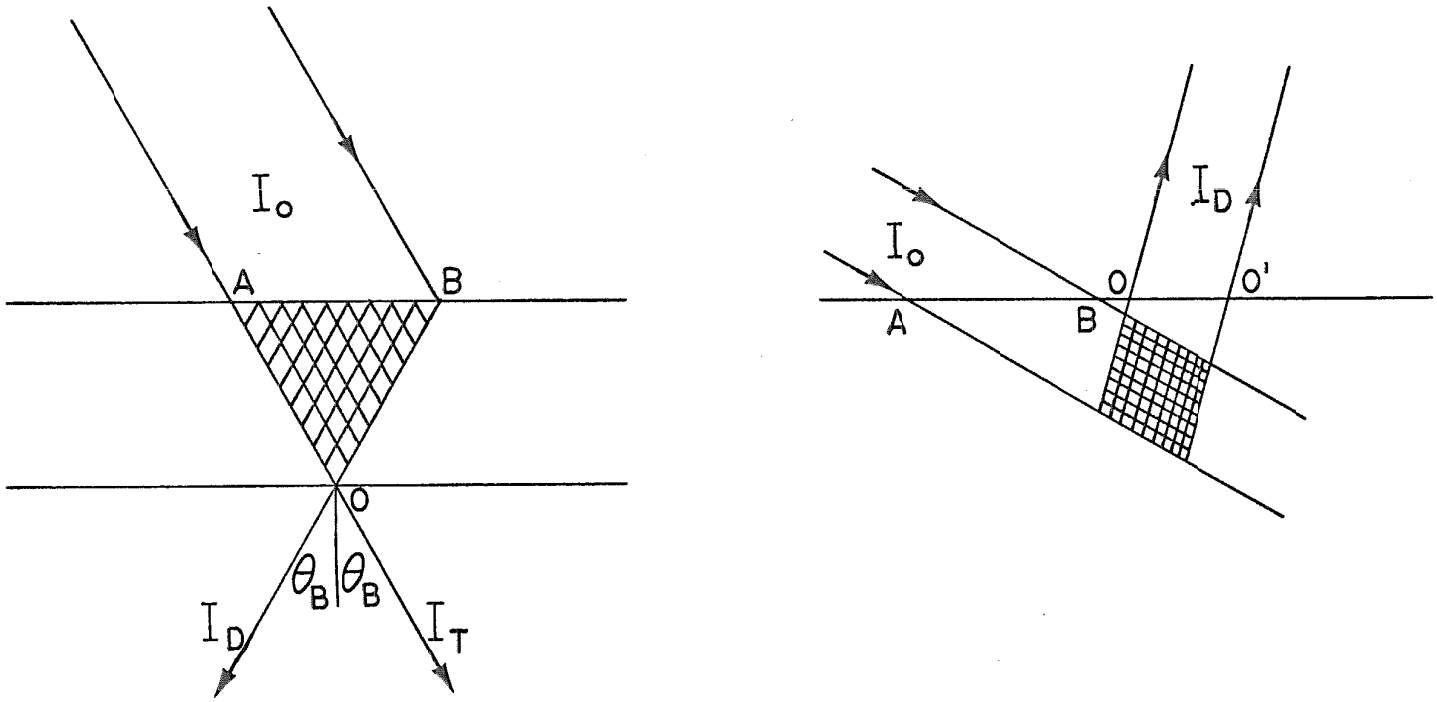

(a) (b)

Figure 15. Diagrams of integration region to obtain solutions for the observed outputs at O or over OO'. The results will be a function of the input intensity I_o over AB, and a function of the strain fields in the grid region.

solution at the nearest neighbor points in the grid and a function of the strain field within the local region of the grid. For the localized strain field of the dislocation, it would probably be best to use a variable dimension finite element mesh to define the strain by region. Near the dislocation the mesh size would be of the order of atom to atom distances, while for regions several microns away from the dislocation, the strain could be considered constant over much larger regions. Several computer simulations have already proved satisfactory in explaining dislocation images in special cases (Balibar and Authier, 1967; Bedynska, 1973; Taupin, 1967). This work must be extended to the intermediate range of absorptions to obtain the complete solution for the present work.

APPENDIX B

Crystal Growth Using a Modified Czochralski Technique

Figure 16 shows a cross-section view of the crystal growing system. The seed pulling rod was attached to a gear system which both rotated the seed at 2 revolutions per minute and raised the seed-crystal at approximately 1 cm of growth per hour. The cylindrical mullite radiation shields, the copper disks on the seed holder, the graphite after-heater, and the graphite disks coupled to the crucible are all required to maintain a steady temperature and a shallow temperature gradient in the growth region. Vertical motion of the tap coil is the direct power controller, allowing for variations in coupling to the main coil. Two viewing ports through the graphite mold and mullite shields, situated 0.5cm above the initial copper surface, provide easy observations of the growth procedure.

One essential condition for growth of highly perfect copper single crystals is purity of materials. All copper, quartz, and mullite parts of the interior of the system were cleaned before each growth cycle by using concentrated nitric acid, rinsing in distilled water and, if possible, vacuum drying at approximately 200 degrees centigrade. The graphite crucible was periodically treated with a high temperature bake in flourine gas to reduce impurity levels of stray metals to less than 5 parts per million. Whenever an impurity

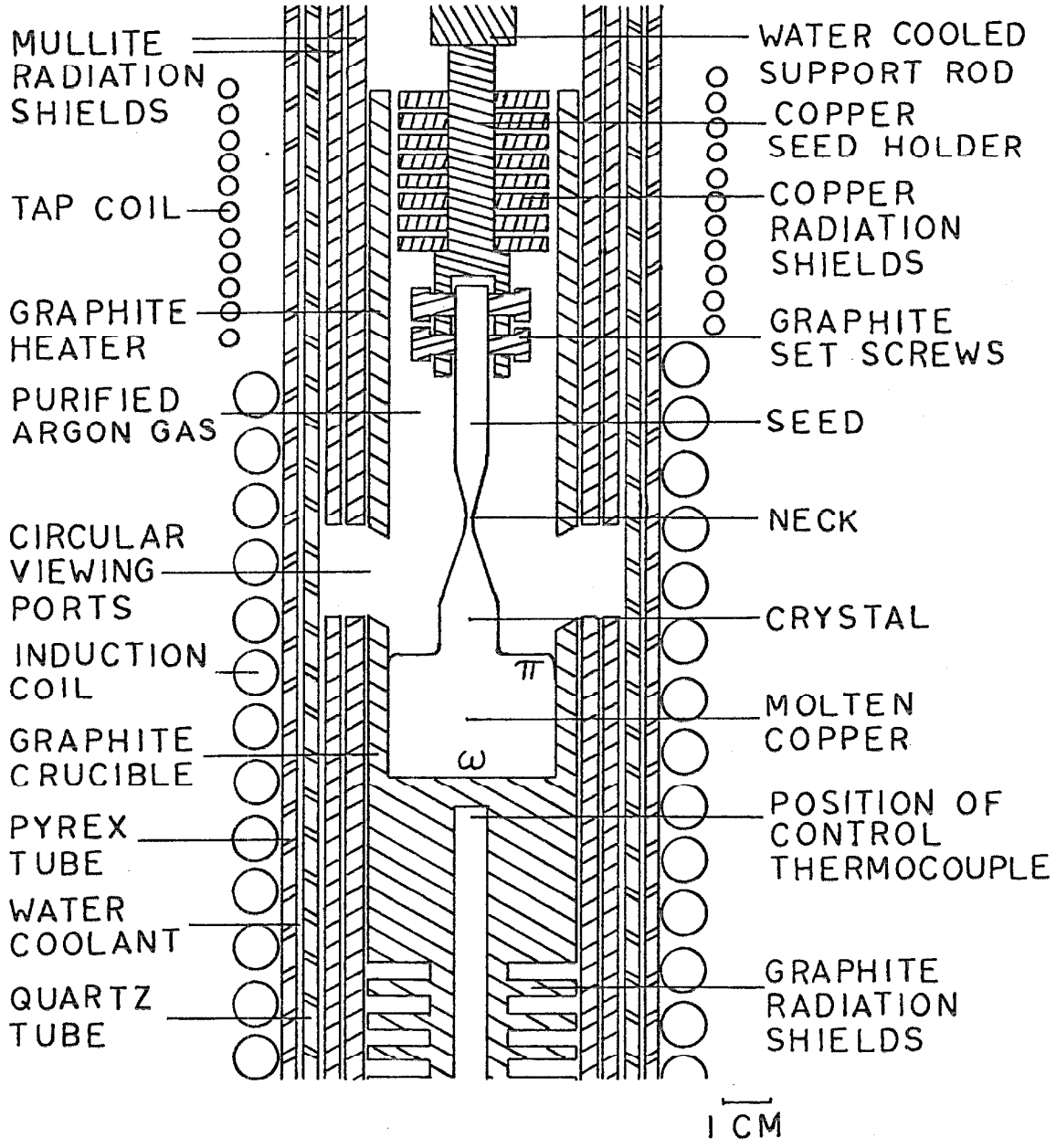

Figure 16. Diagram of crystal growing apparatus showing crystal in process of growth.

layer or crust was observed on the copper melt surface, the growth was usually stopped. The potential preferential solidification at a region marked π in figure 16, due to the impurity on the surface, has on several occasions caused the crystal to grow off center, bump, and damage the seed by twisting the neck. Repurification and a new growth cycle were necessary.

A further pair of critical conditions for growth are the axial temperature gradient and the accuracy of holding a temperature. The gradient should essentially be flat at the base of the melted copper pot, but the gradient at the top cannot be too large. If either the top or bottom of the pot becomes too cool and solidifies, at ω or π in figure 16, bumping of the crystal and twisting can occur as mentioned above. It is estimated that the overall temperature gradient through the growth region is less than 2 degrees Centigrade per centimeter, possibly much less. The afterheater and radiation shields keep this gradient low even with the radiative and conductive heat losses above the melt surface. With such a flat gradient through the growth region, small fluctuations in temperature produce large fluctuations in the solidification conditions. It was found that a change of ¼ degree Centigrade often produced "pagoda" shaped contours on the diameter of the crystal, changing the crystal diameter by 50 to 100 percent (figures 1a and 1b). Obviously, the thermal

strain on the crystal is too great under those conditions to effect a good crystal.

The growth process itself requires a necking of the seed to less than 1mm diameter to reduce the number of dislocations growing in the crystal directly from the seed. As the temperature is increased above the melt temperature, the fluid becomes less viscous and cannot maintain a large meniscus. By carefully raising the temperature to approximately 30 degrees Centigrade above the melt temperature, the seed can be necked or, later, the crystal can be smoothly cut off from the remaining melted copper. Reversing the process smoothly increases the crystal diameter to a useable size of approximately 2cm. To the accuracy of the thermocouples, set in the graphite near the melted copper, the temperature at this point is equal to or slightly below the melt point. It often becomes very clear how close one is to the melt point when a drop of 0.5 degree Centigrade will freeze the entire pot of copper. It is possible that the only obstacle stopping solidification is the need to release the latent heat of the liquid. The growth of a crystal, over approximately ten hours, is completed by a necking process as mentioned or by using the entire supply of copper, approximately 200 grams. The former method is the preferred of the two, since the thermal cooling of the crystal is smoother in that case than when the crystal instantly looses contact with the graphite heat

source in the latter case.

After growth the crystal is hanging vertically from the seed. To remove it from the seed without any undue stresses, a wax boat is set around it in position. The neck is cut by acid dissolving with nitric acid. The crystal can then be set horizontally and a stronger wax support built around it. At this point (Figure 1b) the crystal is ready to be machined into specimens and tested.

Further information on crystal growth by the Czochralski method can be found in Billig (1956), Kuriyama, Boettinger and Burdette (1976), Valentino and Brandle (1974), and Young and Savage (1964). Some information on thermal problems during the growth process may be obtained in Kuriyama, Early, and Burdette (1974a, 1974b), and in Wood (1973a, 1973b, 1973c).

APPENDIX C

Diffraction-Transmission Beam Stereo in Borrmann Topography

It was initially expected that no stereo depths would be observable when the diffracted and transmitted beams were compared. The energy is transmitted through the crystal along the reflecting planes to the exit surface and, at that point, decoupled into diffracted and transmitted beams. All defects would be observed at the same depth with respect to the gold dot images. Such was not the case. There existed relative depths between dislocations which by themselves provided stereo information. The Cottrell-Lomer extended dislocations were observed deeper than the short sharp dislocations as in the asymmetric stereo topographs.

Figure 14 shows the stereo geometry near the exit surface of the crystal required to produce the observed stereo effects. The gold dot image is shifed "into" the crystal due to its strain field. Theory shows that the Bloch wave arriving at the dislocation site may be decoupled into transmitted and diffracted beams, which, if they are sufficiently close to the exit surface, may not be totally absorbed any may exit from the specimen with the stereo information. The information arriving from dislocations deeper than this region, primarily the Cottrell-Lomer dislocations, can also be decoupled in the region near the exit surface of the specimen, but the method by which this takes place is less clear. The

apparent depth, h, of the dislocation is related to the image shift, S, by the equation

$$h = \frac{S}{2 \cdot \tan \theta} = \frac{S_2 - S_1}{2 \tan \theta}$$

and the real depth, H, is given by

$$H = H_o + h = H_o + \frac{S_2 - S_1}{2 \tan \theta}$$

where H_o is the apparent depth of the image of the gold dots, θ is the Bragg angle, and S_1 and S_2 are the distances on the two topographs between the image at the dislocation and the nearest gold dot.

Boettinger, Burdette, Farabaugh, and Kurlyama (1977) have shown that the decoupling of the Bloch wave for small strain takes the form of $\sin(\vec{k} \cdot \vec{u})$, with $\vec{k}$ equal to the diffracted and transmitted direction vectors, and $\vec{u}$ equal to the strain vector. For the gold dot, the atomic mismatch of the epitaxial growth sets the strain field radially outward from the center of the gold dot. Therefore, as observed, the dot image on either the diffracted or transmitted beam will be a light-dark (or dark-light) image in the direction of the plane of incidence. The energy flow through the crystal is disrupted and energy is transferred from the channeling Bloch wave form into the separated beams. Comparing light

to dark images shows that very little total loss of energy is noted. This result is expected when pure mass absorption is assumed for the gold dot.

APPENDIX D

Stereo Geometry Calculations- Berg-Barrett Topography

Figures 2, 3, 12, and 13 provide the necessary geometrical information for evaluating the stereo angles and image shifts in the Berg-Barrett system. By combining the following calculations with data on the Bragg angle, θ_B, the angle between the reflecting planes and the surface planes, ϕ, and the rolled angle (about the normal to the surface), χ, the stereo angles, $2\beta_r$, and $2\beta_e$, can be determined. In Figure 3, $2\beta_r$ is equal to the angle C_1OC_2 and $2\beta_e$ is equal to angle $\alpha o \beta$.

Figure 3 shows a complete Bragg cone for the 220 reflection from a (111) surface in copper as well as a portion of the $2\bar{2}0$ reflection cone. A planar cut through the origin and including the [110] direction intersects the cone along BO and OC, the directions defining the incoming and reflected X-ray beams. Without loss of generality, one can assume a unit cone by setting

$$OB_1 = OB_2 = OC_1 = OC_2 = 1$$

Angles BOA and COA are equal to $90^o\theta_B$.

Angle AOH, the interplanar angle, is equal to ϕ.

Angle I_1OI_2 is twice the rolled angle, 2ψ, which is also equal to angle B_1GB_2.

Some geometrical lengths necessary for further calculations are obtained immediately and detailed as follows:

$$OA = \cos(90° - \Theta_B) \qquad AB = AC = \sin(90° - \Theta_B)$$

$$AD = AE = AB(\cos\alpha) = \sin(90° - \Theta_B)\cos\alpha$$

$$BD = CE = AB\sin\alpha = \sin(90° - \Theta_B)\sin\alpha$$

$$AF = OA\tan\phi = \cos(90° - \Theta_B)\tan\phi$$

$$EF = EA - AF = \sin(90° - \Theta_B)\cos\alpha - \cos(90 - \Theta_B)\tan\phi$$

$$DF = AF + AD = \sin(90° - \Theta_B)\cos\alpha + \cos(90° - \Theta_B)\tan\phi$$

$$OF = OA/\cos\phi = \cos(90° - \Theta_B)/\cos\phi$$

$$HD = DF\cos\phi = \cos\phi[\sin(90° - \Theta_B)\cos\alpha + \cos(90° - \Theta_B)\tan\phi]$$

With the above lengths for Figure 3, one proceeds as follows: Obtain angle BAD, α, as a function of ψ, the rolled angle.

$$\tan\psi = \frac{BD}{HD} = \frac{\sin(90° - \Theta_B)\sin\alpha}{\cos\phi[\sin(90° - \Theta_B)\cos\alpha + \cos(90° - \Theta_B)\tan\phi]} \qquad \text{(D-0)}$$

Solving for $\sin\alpha$ yields

$$\sin^2\alpha[1 + \tan^2\psi\cos^2\phi] - \sin\alpha \frac{2\tan\psi\sin\phi}{\tan(90° - \Theta_B)} + \frac{\tan^2\psi\sin^2\phi}{\tan 2(90° - \Theta_B)} - \tan^2\psi\cos^2\phi = 0 \qquad \text{(D-1)}$$

The positive root is the root of interest here.

Angle CHE, or χ, can now be determined, given α, from

$$\tan\chi = \frac{CE}{EH}$$

where

$$EH = EF\cos\phi = \cos\phi\{\sin(90°-\theta_B)\cos\alpha - \cos(90°-\theta_B)\tan\phi\}$$

Thus

$$\tan\chi = \frac{\sin(90°-\theta_B)\sin\alpha}{\cos\phi\{\sin(90°-\theta_B)\cos\alpha - \cos(90°-\theta_B)\tan\phi\}} \qquad (D\text{-}2)$$

Both angle C_1OC_2, $2\beta_r$, and angle C_1OH, β, can be evaluated from

$$\sin\beta_r = \frac{CE}{OC} = \sin(90°-\theta_B)\sin\alpha$$

$$2\beta_r = 2\arcsin(\sin(90°-\theta_B)\sin\alpha) \qquad (D\text{-}3)$$

and

$$\beta = \arcsin(CH/OC) = \arcsin\{\frac{\cos\phi}{\cos\chi}[\sin(90°-\theta_B)\cos\alpha - \cos(90°-\theta_B)\tan\phi]\} \qquad (D\text{-}4)$$

Using the geometry of the two reflections, 220 and 202, the stereo angle for the extinction pairs, $2\beta_e$, is derived from β by

$$\sin\beta_e = \sin\beta\sin\rho$$

where ρ is the rotation angle in the surface plane between the stereo topograph pairs. The rotation angle between pairs is 120° in this case, so

$$\sin\beta_e = \frac{\sqrt{3}}{2}\sin\beta$$

and

$$2\beta_e = 2\arcsin\left(\frac{\sqrt{3}}{2}\sin\beta\right) \qquad \text{(D-5)}$$

Solving equations D-1 through D-5 for any system immediately provides the two required stereo angles, $2\beta_r$ and $2\beta_e$.

Stereo Geometry Calculations - Transmission Topography

In the diffracted-transmitted Borrmann stereo topographs, it is directly observed (Figure 4b) that the stereo angle is $2\theta_B$, where θ_B is the Bragg angle of the reflection. In the present work with copper $K_{\alpha 1}$ radiation reflecting off $(2\bar{2}0)$ planes in a [111] oriented copper specimen, the stereo angle is twice the Bragg angle, or 74.12°.

It is a very simple extension of the reflection topography calculations described in the previous section to calculate the stereo angle for rolled transmission topographs, as in Figure 4a. By considering ϕ, the interplanar angle, to be equal to 90°, equation D-1 is incorrect since equation D-0 is undefined. However, the simple geometry of both Figures 3 and 4a will show that $\alpha=\psi$ if, in the transmission geometry, one rotates the [111] crystal to the asymmetric points about the $[1\bar{1}0]$ direction. This leads directly to the stereo angle formula

$$2\beta_r = 2\arcsin(\sin(90°-\theta_B)\sin\alpha)$$

as computed for the Berg-Barrett topographs.

REFERENCES

1. M. Ashkin and M. Kuriyama, "Quantum Theory of X-ray Diffraction by a Crystal", J. Phys. Soc. Japan 21, 1549, (1966).

2. A. Authier, "Contrast of Dislocation Images in X-ray Transmission Topography", Denver Conference on X-ray Analysis, 1966.

3. F. Balibar and A. Authier, "Etude Theorique et Experimentale du Contraste des Images de Dislocations", Phys. Stat. Sol. 21, 413, (1967).

4. T. Bedynska, "Contrast of Dislocation Image in the Bragg Case", Phys. Stat. Sol. 18, 147, (1973).

5. E. Billig, "Some Defects in Crystals Grown from the Melt", Proc. Royal Soc. A 235, 37, (1956).

6. W.J. Boettinger, H.E. Burdette, E.N. Farabaugh, and M. Kuriyama, "Some Topographic Observations of the Effects of Dynamical Diffraction in Imperfect Metal Crystals". Advan. in X-ray Anal., to be published, (1977).

7. W.J. Boettinger, H.E. Burdette, and M. Kuriyama, "Applications of Contrast Conditions to Dynamical Images of Immobile Dislocations", Phil. Mag. 34, 119, (1976).

8. H. Fehmer and W. Uelhoff, "Die Zuchtung Versetzungfreier Kupfereinkristalle", J. Crystal Growth 13/14, 257, (1972).

9. K. Haruta, "New Methods of Obtaining Stereoscopic Pairs of X-ray Diffraction Topographs", J. Appl. Phys. 36, 1789, (1965).

10. M. Hayashi and T. Shichiri, "Theoretical and Experimental Study of the Growth of Perfect Crystals", J. Crystal Growth 21, 254, (1974).

11. K.M. Jassby and T. Vreeland, Jr., "An Experimental Study of the Mobility of Edge Dislocations in Pure Copper Single Crystals", Phil. Mag. 21, 1147, (1970).

12. K.M. Jassby and T. Vreeland, Jr., "Dislocation Mobility in Pure Copper at 4.2 K", Phys. Rev. B 8, 3537, (1973).

13. M. Kuriyama, "Theory of X-ray Diffraction by a Distorted Crystal", J. Phys. Soc. Japan 23, 1369, (1967), J. Phys. Soc. Japan 25, 846, (1968).

14. M. Kuriyama, "The Dynamical Scattering Amplitude of an Imperfect Crystal", Acta Cryst. A25, 56, (1969a), Acta Cryst. A28, 588, (1972), Acta Cryst. A30, 525 (1974).

15. M. Kuriyama, "X-ray Diffraction from a Crystal Containing Isolated Imperfections", Acta Cryst. A25, 682, (1969b).

16. M. Kuriyama, "On the Principle of X-ray Interferometry", Acta Cryst. A27, 273, (1971).

17. M. Kuriyama, "Dynamical Diffraction Equations for Imperfect Crystals", Zeits. fur Naturf. 28a, 622, (1973).

18. M. Kuriyama, "A Classical Derivation of the Dynamical Diffraction Equation for Imperfect Crystals Based on the Ewald-Laue-Bethe Theory", Acta Cryst. A31, 774 (1975).

19. M. Kuriyama, W.J. Boettinger, and H.E. Burdette, "Crystal Perfection in Czochralski Growth", NBSIR 74-611, 3, (1974), NBSIR 76-980, 3, (1976).

20. M. Kuriyama, J.G. Early, and H.E. Burdette, "Characterization of Thermal Convection and Crystal Perfection in Metals Grown from the Melt", NBS Reports 10-873, (1972).

21. M. Kuriyama, J.G. Early, and H.E. Burdette, "Effects of Convection on Crystal Perfection in Czochralski Crystal Growth", NBSIR 73-402, 3, (1973).

22. M. Kuriyama, J.G. Early, and H.E. Burdette, "An Immobile Dislocation Arrangement in As-Grown Copper Single Crystals Observed by X-ray Topography", J. Appl. Cryst. 7, 535 (1974a).

23. M. Kuriyama, J.G. Early, and H.E. Burdette, "Fluid Flow Effects on Crystalline Perfection", AIAA paper number 74-204, (1974b).

24. M. Kuriyama and T. Miyakawa, "Primary and Secondary Extinctions in the Dynamical Theory for an Imperfect Crystal", Acta Cryst. A26, 667, (1970).

25. A.R. Lang, "Direct Observations of Individual Dislocations by X-ray Diffraction", J. Appl. Phys. 29, 597, (1958).

26. A. R. Lang, "Studies of Individual Dislocations in Crystals by X-ray Diffraction Microradiography", J. Appl. Phys. 30, 1748, (1959a).

27. A.R. Lang, "The Projection Topograph: A New Method of X-ray Diffraction Microradiography", Acta Cryst. 12, 249, (1959b).

28. J.D. Livingston, "Etch Pits at Dislocations in Copper". J. Appl. Phys. 31, 1071, (1960).

29. M.C. Narasimhan and B. Roessler, "A New X-ray Topographic Technique: The Narrow Line Focus Sweep", unpublished, (a).

30. M.C. Narasimhan and B. Roessler, "Stereoscopic Imaging of Dislocations by Anomalous Transmission X-ray Topography", unpublished, (b).

31. J.B. Newkirk, "The Observations of Dislocations and Other Imperfections by X-ray Extinction Contrast", Trans. TMS-AIME 215, 483, (1959).

32. P. Penning and D. Polder, "Anomalous Transmission of X-rays in Elastically Deformed Crystals", Philips Research Reports 16, 419, (1961).

33. D. Polder and P. Penning, "Anomalous Transmission of X-rays in an Elastically Deformed Non-Isotropic Crystal", Acta Cryst. 17, 950, (1964).

34. D.B. Pope, "The Mobility of Edge Dislocations In the Basal Slip Systems of Zinc", Ph.D. Thesis, California Institute of Technology (1967).

35. D.B. Pope and T. Vreeland, Jr., "Basal Dislocation Density Measurements in Zinc", Trans. TMS-AIME 245, 2447, (1969).

36. B. Roessler and R.W. Armstrong, "Dynamical Theory Approach to Berg-Barrett Technique", Advan. in X-ray Anal. 12, 139, (1968).

37. T. Saka, T. Katagawa, and N. Kato, "The Theory of X-ray Crystal Diffraction for Finite Polyhedral Crystals", Acta Cryst. A28, 102, (1972a), Acta Cryst. A28, 113, (1972b), Acta Cryst. A29, 192, (1973).

38. C.H. Sworn and T.E. Brown, "The Growth of Dislocation-Free Copper Crystals", J. Crystal Growth 15, 195, (1972).

39. S. Takagi, "Dynamical Theory of Diffraction Applicable to Crystals with Any Kind of Small Distortion", Acta Cryst. 15, 1311, (1962).

40. S. Takagi, "A Dynamical Theory of Diffraction for a Distorted Crystal", J. Phys. Soc. Japan 26, 1239, (1969).

41. B.K. Tanner, "The Perfection of Czochralski-Grown Copper Single Crystals", J. Crystal Growth 16, 86, (1972).

42. D. Taupin, "Prevision de Quelques Images de Dislocations par Transmission des Rayons X (Cas de Laue Symetrique)", Acta Cryst. 23, 25, (1967).

43. L.K. Tu and T. Vreeland, Jr., "A Technique for Berg-Barrett Stereo Topography", Acta Cryst. A30, 852, (1974).

44. A.P. L. Turner, T. Vreeland, Jr., and D. B. Pope, "Experimental Techniques for Observing Dislocations by the Berg-Barrett Method", Acta Cryst. A24, 452, (1968).

45. A.J. Valentino and C.D. Brandle, "Diameter Control of Czochralski Grown Crystals", J. Crystal Growth 26, 1, (1974).

46. T. Vreeland, Jr., "Stereographic X-ray Reflection Topography of Dislocations in Zinc", J. Appl. Cryst. 9, 34, (1976).

47. D.S. Wood, "The Temperature Distribution in a Solid Which Produces no Thermal Stress", unpublished, (1973a).

48. D.S. Wood, "The Influence of Impurities upon the Growth of Crystals of High Perfection", unpublished (1973b).

49. D.S. Wood, "The Temperature in a Crystal During Solidification from the Melt", unpublished, (1973c).

50. E.W. Young, Jr., and J. R. Savage, "Growth of Copper Crystals of Low Dislocation Density", J. Appl. Phys. 35, 1917, (1964).